

Precipitation Growth Processes in the Comma-Head Region of the 7 February 2020 Northeast Snowstorm: Results from IMPACTS

MEGAN M. VARCIE,^a TROY J. ZAREMBA,^a ROBERT M. RAUBER,^a GREG M. MCFARQUHAR,^{b,c} JOSEPH A. FINLON,^d LYNN A. MCMURDIE,^d ALEXANDER RYZHKOV,^{b,e} MARTIN SCHNAITER,^f EMMA JÄRVINEN,^f FRITZ WAITZ,^f DAVID J. DELENE,^g MICHAEL R. POELLOT,^g MATTHEW L. WALKER MCLINDEN,^h AND ANDREW JANISZESKI^a

^a Department of Atmospheric Sciences, University of Illinois Urbana–Champaign, Urbana, Illinois

^b Cooperative Institute for Severe and High-Impact Weather Research and Operations, University of Oklahoma, Norman, Oklahoma

^c School of Meteorology, University of Oklahoma, Norman, Oklahoma

^d Department of Atmospheric Sciences, University of Washington, Seattle, Washington

^e NOAA/OAR/National Severe Storms Laboratory, Norman, Oklahoma

^f Institute of Meteorology and Climate Research, Karlsruhe Institute of Technology, Eggenstein–Leopoldshafen, Germany

^g Department of Atmospheric Sciences, University of North Dakota, Grand Forks, North Dakota

^h NASA Goddard Space Flight Center, Greenbelt, Maryland

(Manuscript received 20 May 2022, in final form 23 August 2022)

ABSTRACT: On 7 February 2020, precipitation within the comma-head region of an extratropical cyclone was sampled remotely and in situ by two research aircraft, providing a vertical cross section of microphysical observations and fine-scale radar measurements. The sampled region was stratified vertically by distinct temperature layers and horizontally into a stratiform region on the west side, and a region of elevated convection on the east side. In the stratiform region, precipitation formed near cloud top as side-plane, polycrystalline, and platelike particles. These habits occurred through cloud depth, implying that the cloud-top region was the primary source of particles. Almost no supercooled water was present. The ice water content within the stratiform region showed an overall increase with depth between the aircraft flight levels, while the total number concentration slightly decreased, consistent with growth by vapor deposition and aggregation. In the convective region, new particle habits were observed within each temperature-defined layer along with detectable amounts of supercooled water, implying that ice particle formation occurred in several layers. Total number concentration decreased from cloud top to the -8°C level, consistent with particle aggregation. At temperatures $> -8^{\circ}\text{C}$, ice particle concentrations in some regions increased to $>100\text{ L}^{-1}$, suggesting secondary ice production occurred at lower altitudes. WSR-88D reflectivity composites during the sampling period showed a weak, loosely organized banded feature. The band, evident on earlier flight legs, was consistent with enhanced vertical motion associated with frontogenesis, and at least partial melting of ice particles near the surface. A conceptual model of precipitation growth processes within the comma head is presented.

SIGNIFICANCE STATEMENT: Snowstorms over the northeast United States have major impacts on travel, power availability, and commerce. The processes by which snow forms in winter storms over this region are complex and their snowfall totals are hard to forecast accurately because of a poor understanding of the microphysical processes within the clouds composing the storms. This paper presents a case study from the NASA IMPACTS field campaign that involved two aircraft sampling the storm simultaneously with radars, and probes that measure the microphysical properties within the storm. The paper examines how variations in stability and frontal structure influence the microphysical evolution of ice particles as they fall from cloud top to the surface within the storm.


KEYWORDS: Extratropical cyclones; Snowbands; Cloud microphysics

1. Introduction

The comma-head region of extratropical cyclones over the midwestern and eastern United States have been shown in both observational and modeling studies to often exhibit an elevated layer of potential instability and convection on their equatorward (warm) sides, and stable air, often topped by shallow convective cloud-top generating cells on their poleward

(cold) sides (Wiesmueller and Zubrick 1998; Martin 1998; Nicosia and Grumm 1999; Novak et al. 2008, 2009; Rauber et al. 2014; Rosenow et al. 2014). Studies have also shown that the elevated potential instability is associated with the intrusion of dry air over the cyclones' warm front, the dry air originating within the cyclones' dry slot (e.g., Han et al. 2007; Grim et al. 2007; Rauber et al. 2014; Rosenow et al. 2014).

Research on the microphysical structure of the comma-head region, and the relationship of microphysical processes to mesoscale storm dynamics and precipitation bands within the comma head, has focused on storms over the Pacific Northwest associated with the Cyclonic Extratropical Storm Project (CYCLES) and the Improvement of Microphysical Parameterization through Observational Verification Experiment

 Denotes content that is immediately available upon publication as open access.

Corresponding author: Robert M. Rauber, r-rauber@illinois.edu

DOI: 10.1175/JAS-D-22-0118.1

© 2022 American Meteorological Society. For information regarding reuse of this content and general copyright information, consult the [AMS Copyright Policy \(www.ametsoc.org/PUBSReuseLicenses\)](https://www.ametsoc.org/PUBSReuseLicenses).

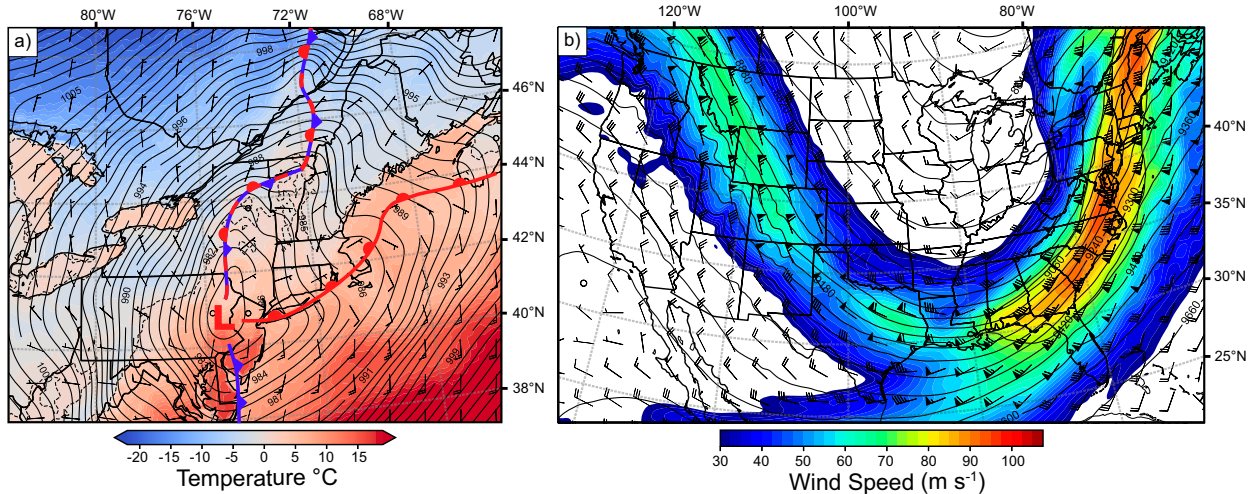


FIG. 1. RAP analysis valid at 1500 UTC 7 Feb 2020: (a) 2-m temperature shaded ($^{\circ}\text{C}$), mean sea level pressure (1-hPa contours), and 10-m winds (m s^{-1}); (b) 300-hPa heights (60-m contours), and wind speed (m s^{-1} , shaded). Wind barb convention: half barb = 5 m s^{-1} , full barb = 10 m s^{-1} , and flag = 50 m s^{-1} . Frontal boundaries are based on subjective analysis of the 2-m temperature, sea level pressure, and 10-m winds. Fronts use standard depictions for cold, warm, and stationary fronts.

(IMPROVE-1) campaigns (e.g., Houze et al. 1976a,b, 1979, 1981; Matejka et al. 1980; Hobbs et al. 1980; Herzegh and Hobbs 1980, 1981; Evans et al. 2005), and over the central United States during the Profiling of Winter Storms (PLOWs) campaign (e.g., Plummer et al. 2014, 2015; Murphy et al. 2017). Outside of these geographic regions, studies of the microphysical structure of cold-season continental cyclones, and other winter cloud systems not associated with cyclones, have focused on the low-level production of supercooled water (e.g., Guan et al. 2001; Cober et al. 2001), processes leading to formation and depletion of supercooled water (Rasmussen et al. 1992), the prolonged existence of mixed-phase clouds (e.g., Cober et al. 2001; Vaillancourt et al. 2003; Korolev and Isaac 2006), and feedbacks on dynamics due to latent cooling at the melting layer (e.g., Szeto and Stewart 1997). There are also limited studies reporting the size distributions of solid hydrometeors in Midwest winter cyclones (Passarelli 1978a,b) and in other winter storms (Gunn and Marshall 1958).

Microphysical investigations in winter storms along the U.S. East Coast are limited, despite these storms' prevalence and impact. Recent studies have been confined to surface and remote sensing observations. Stark et al. (2013) analyzed surface microphysical observations within two banded winter cyclones and characterized preband, mature-band, and post-band microphysics, finding a rapid transition in ice particle habits, riming, and snow densities as snowbands passed over the observing location. They also noted the presence of generating cells and referenced their relationship to increased precipitation at the surface. Colle et al. (2014) expanded upon this by presenting surface microphysics observations collected in 12 cyclones over 3 winter seasons. Habit and riming characteristics were analyzed in the context of their spatial location relative to the cyclone low pressure centers. The influence of generating cells and elevated convection on microphysical

processes through different growth layers in East Coast winter storms has yet to be explored, although radar studies examining generating cells have been conducted in this geographic region using vertically pointing radars since the 1950s (e.g., Marshall 1953; Wexler and Atlas 1959). More recently, Rauber et al. (2017) used an airborne W-band radar to investigate a Northeast cyclone finding several distinct substructures such as generating cells and elevated convection. Kumjian and Lombardo (2017) investigated the radar polarization characteristics of six Northeast winter storms using quasi-vertical profiles (e.g., Ryzhkov et al. 2016), showing distinct changes in reflectivity, differential reflectivity, and differential phase across the dendritic growth layer, and rapid changes in melting-layer height over short time scales.

Increasing interest in the physics and dynamics of banded precipitation, the dynamics and thermodynamics of cloud top and elevated convective substructures, the lack of in situ

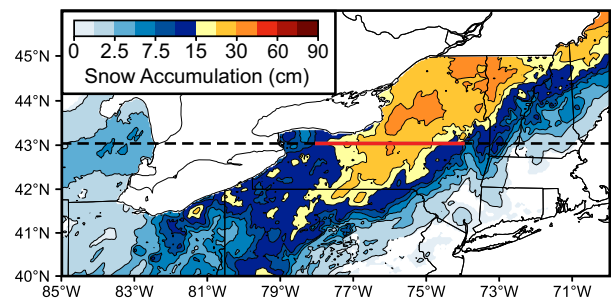


FIG. 2. The 24-h snowfall ending 0000 UTC 8 Feb 2020 (NOHRSC 2022). The dashed black line represents the cross sections in Figs. 4 and 5. The red line represents the flight track location of the ER-2 and P-3 through central New York and the cross sections in Figs. 6, 9, and 10.

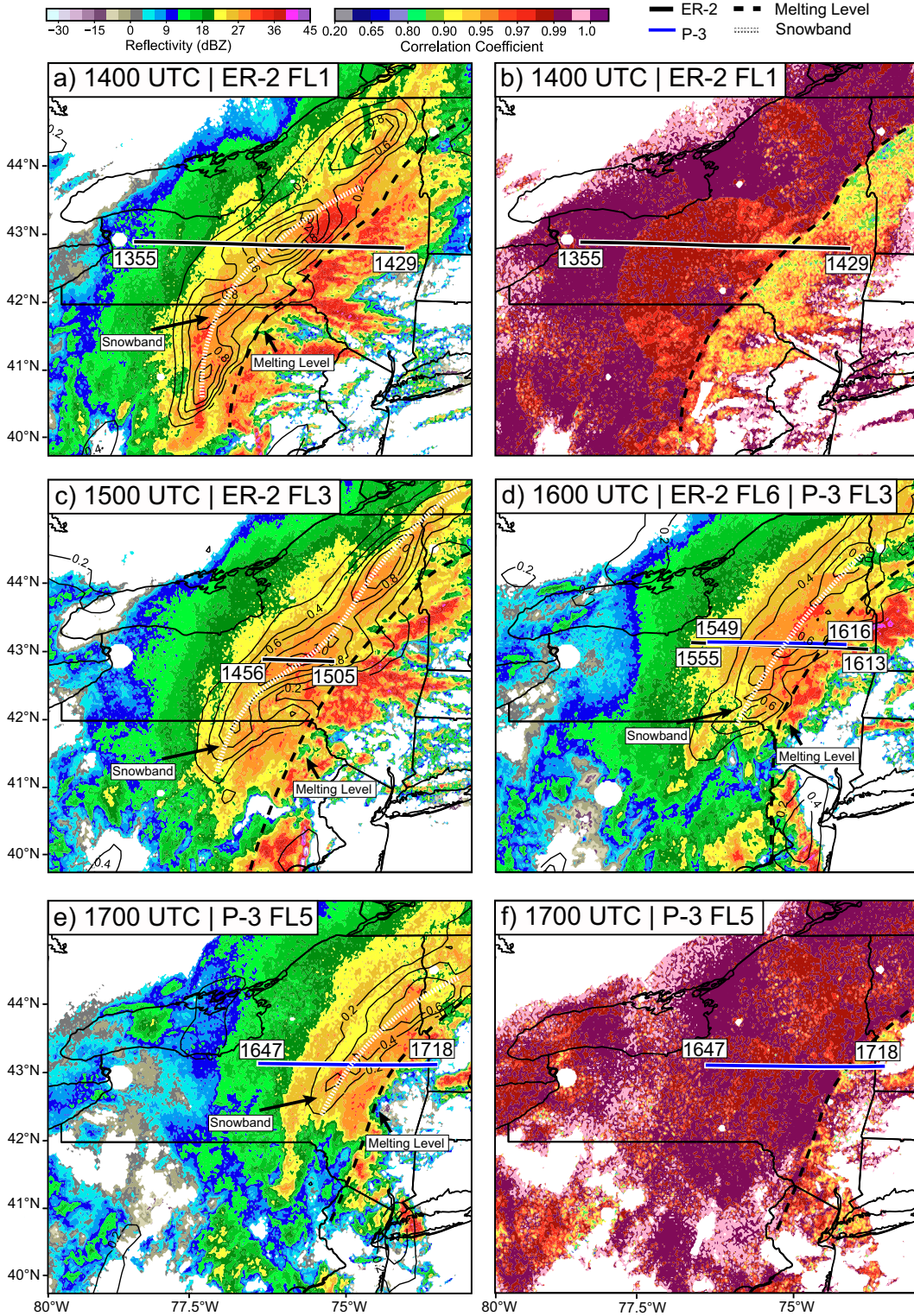


FIG. 3. WSR-88D 2.5-km composites of Z_e and 700-hPa kinematic frontogenesis [$K^{-1} (100 \text{ km})^{-1} (3 \text{ h})^{-1}$; contoured] from RAP analysis for (a) 1400, (c) 1500, (d) 1600, and (e) 1700 UTC 7 Feb 2020. WSR-88D correlation coefficient for (b) 1400 and (f) 1700 UTC 7 Feb 2020. The white dashed lines in (a), (c), (d), and (e) represent the axis of the mesoscale snowband discussed in the text. The black dashed lines in (a)–(e) represent the location of the melting level at 2.5 km subjectively determined using the correlation coefficient. The black line in (a)–(d) is the flight track of the ER-2 and blue line in (d)–(f) is the flight track of the P-3. Flight legs (FL) are labeled.

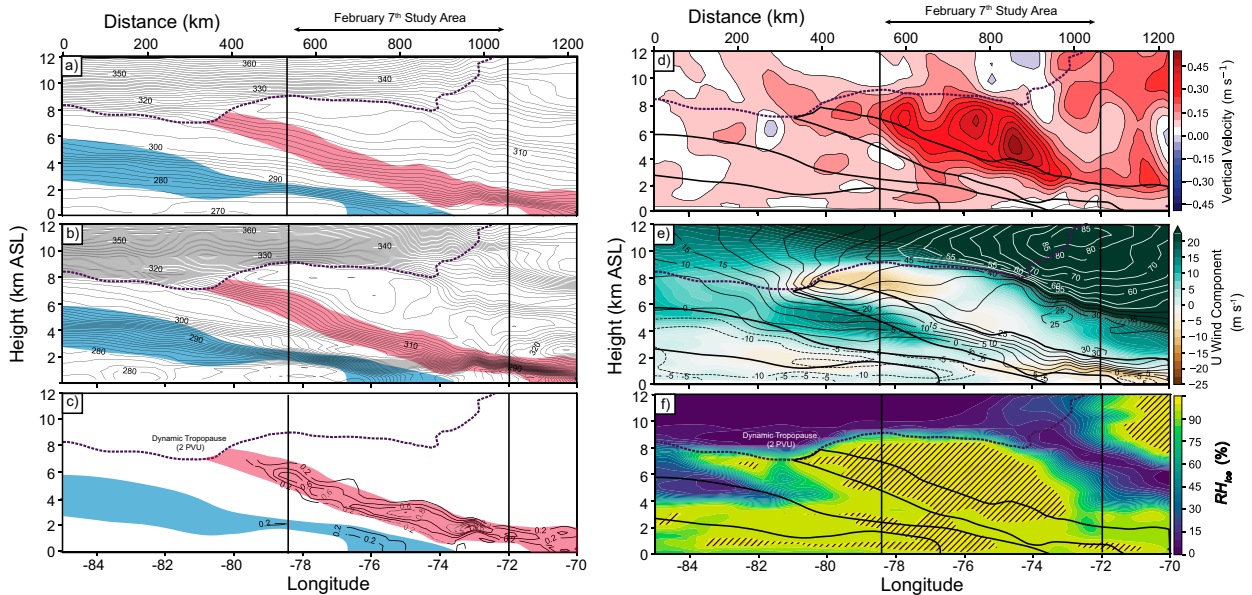


FIG. 4. RAP analysis cross sections along flight tracks at 42.9° latitude between -85° and -65° longitude valid at 1500 UTC 7 Feb 2020. (a)–(c) The stationary frontal zone is shaded in blue and the warm-frontal zone is shaded in red. (d)–(f) These regions are outlined by black solid lines. The vertical black lines represent the study area sampled by the ER-2 and P-3. The dashed black line is the dynamic tropopause (2 PVU). (a) θ (K). (b) θ_e (K). (c) Kinematic frontogenesis in $\text{K}^{-1} (100 \text{ km})^{-1} (3 \text{ h})^{-1}$. (d) Model updraft strength (w) (m s^{-1}). (e) The u component of the wind is shaded and the v component of the wind is contoured (m s^{-1}) (white contours for wind speeds greater than 55 m s^{-1} for clarity). The dashed contours represent winds coming out of the page and solid contours represent winds into the page. (f) Relative humidity with respect to ice (RH_{ice}). Hatched regions denote $\text{RH}_{\text{ice}} > 100\%$.

microphysical observations to characterize these features, and societal impacts of recent winter storms along the East Coast of the United States motivated the National Aeronautics and Space Administration (NASA) Investigation of Microphysics and Precipitation for Atlantic Coast-Threatening Snowstorms (IMPACTS; [McMurdie et al. 2022](#)) field campaign. IMPACTS employed a modern suite of instruments aboard the NASA P-3 Orion (P-3) and the NASA Earth Resources 2 (ER-2) aircraft to collect in situ microphysics and airborne radar data within the comma-head region of Atlantic Coast cyclones. The 7 February 2020 event had the best coordination between the P-3 and ER-2 aircraft during the 2020 deployment. The comma head was characterized by both stratiform and convective regions and provided an opportunity to investigate the microphysical processes within these regions through the depth of the storm. In this paper, microphysical processes are analyzed in the context of the storm's thermodynamic, frontal, and radar structures in order to differentiate the microphysical evolution that occurs with depth between the aircraft flight levels within the stratiform and convective regions of the storms' comma head, and within the banded features evident in the low-level reflectivity field.

The paper is organized as follows: [Section 2](#) provides an overview of the extratropical cyclone's frontal and airmass structure, [section 3](#) provides a discussion of IMPACTS aircraft operations on 7 February 2020, [section 4](#) describes the stability and moisture characteristics across the sample region,

and [section 5](#) describes how the microphysical characteristics varied with depth between the aircraft flight levels in temperature defined particle growth layers. [Section 6](#) discusses the nature of precipitation bands evident on radar. Key findings are summarized in [section 7](#).

2. Storm overview

The 7 February 2020 cyclone developed during the early morning hours as a result of rapid cyclogenesis on the leeward side of the Appalachian Mountains. Rapid cyclogenesis was enhanced by the phasing of two midlevel shortwaves into a negatively tilted trough, resulting in the development of a low over southeast Pennsylvania ([Fig. 1a](#)). Coupled jet streak dynamics and subsequent phasing of the subtropical and polar jet streams into a single jet streak with wind speeds $> 100 \text{ m s}^{-1}$ at 300 hPa across eastern New York were responsible for the rapid intensification of the surface low ([Fig. 1b](#)). Within the 12-h period between 1200 UTC 7 February and 0000 UTC 8 February the surface low pressure center deepened from a mean sea level pressure of 980 to 966 hPa. As the surface low strengthened, well-defined surface frontal boundaries were evident. A surface cold front extended south along the Atlantic Coast, while a surface warm front extended east from the center of the low. A preexisting stationary front extended northward from the low pressure center across central New York ([Fig. 1a](#)). The IMPACTS flights sampled the storm across the stationary front between 1400 and 1800 UTC during this period of deepening (see flight track

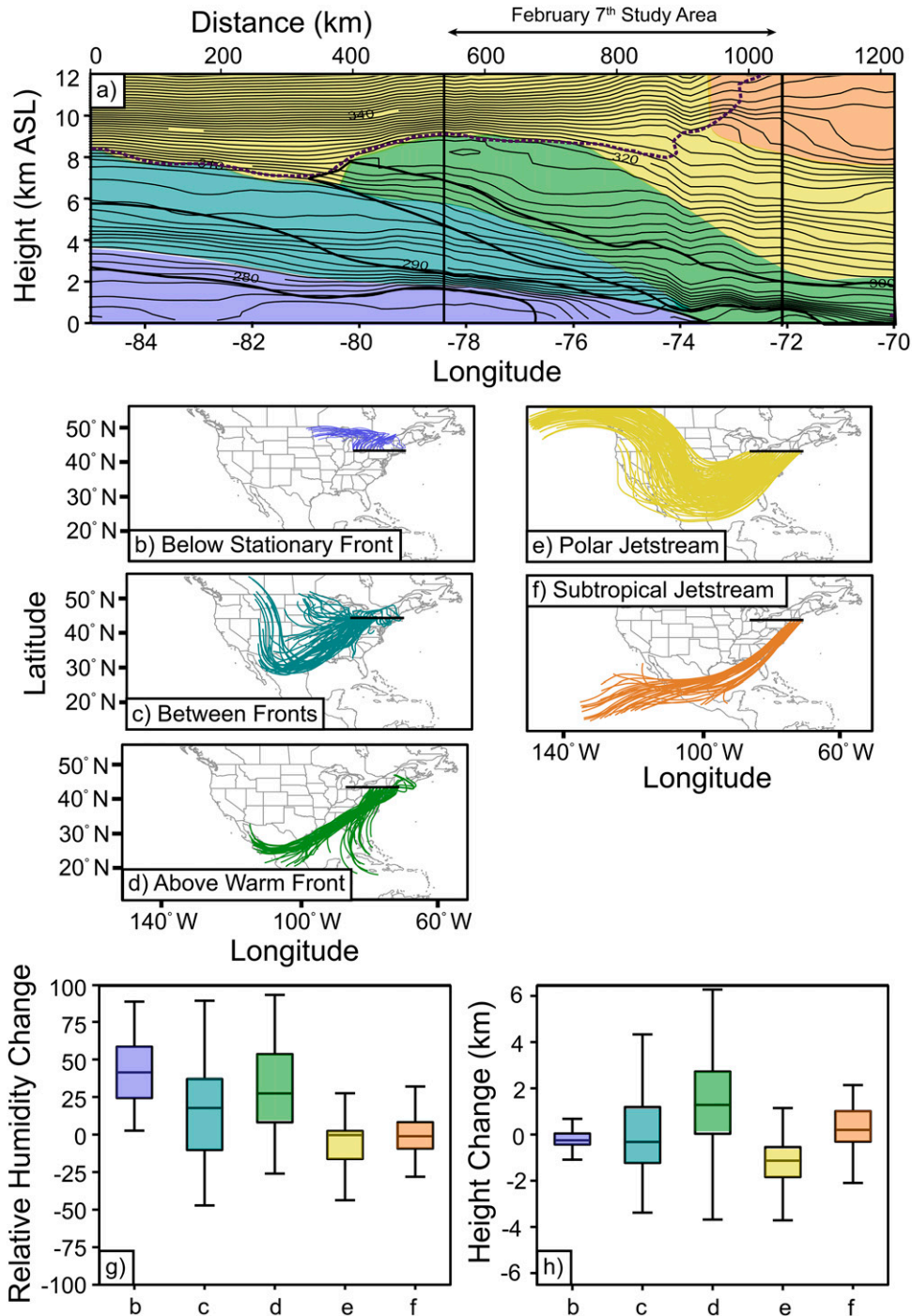


FIG. 5. Cross section showing ending points (in time) of 48-h HYSPLIT back trajectories calculated using 12-km NAM data valid at 1500 UTC 7 Feb 2020. (a) Colors correspond to trajectories coming from (b)–(f) various source regions. θ (K) from RAP analysis valid at 1500 UTC is overlaid over the different air masses. (b) Blue trajectories represent air beneath the stationary front. (c) Teal trajectories represent air between the stationary and warm front. (d) Green trajectories represent air above the warm front. (e) Yellow trajectories represent air associated with the polar jet stream. (f) Orange trajectories represent air associated with the subtropical jet stream. (g) Change in relative humidity with respect to water (RH_{Water}) between the start and end points of the trajectories. (h) Change in height (km) between the start and end points of the trajectories associated with different air masses. Letters and boxplot colors correspond to the panels above. Boxes represent the 25th, 50th, and 75th percentiles. Whiskers represent the maximum and minimum data points.

TABLE 1. Sampling characteristics of each P-3 flight leg. Coordinated flight legs with the ER-2 are in boldface. Temperature layers sampled include the dendritic growth layer (DGL), plate growth layer (PGL), needle growth layer (NGL), and enhanced aggregation layer (EAL).

Flight leg	Time (UTC)	Direction	Altitude (km)	Temperature (°C)	Temperature layer sampled
Stratiform region					
1	1503:50–1512:02	West–east	5.2	–15.9 to –15.0	DGL
2	1537:18–1549:20	East–west	3.6	–12.2 to –8.3	PGL
3	1552:00–1606:25	West–east	3.3	–12.8 to –7.3	PGL, NGL
5	1647:10–1703:16	West–east	2.7	–6.6 to –4.5	NGL
4	1628:18–1643:20	East–west	2.4	–5.0 to –2.8	NGL
Convective region					
1	1512:02–1522:50	West–east	5.2	–15.6 to –13.9	DGL
2	1526:40–1537:18	East–west	3.6	–8.6 to –5.4	PGL, NGL
3	1606:25–1613:40	West–east	3.3	–7.7 to –2.2	NGL, EAL
5	1703:16–1718:20	West–east	2.7	–5.0 to –0.7	NGL, EAL
4	1617:20–1628:18	East–west	2.4	–3.7 to –0.2	NGL, EAL

plotted in Fig. 2). Twenty-four-hour snow accumulations of nearly 20–30 cm (7.8–11.8 in.) were recorded over west and central New York State by 0000 UTC 8 February (Fig. 2).

Weather Surveillance Radar-1988 Doppler (WSR-88D) equivalent reflectivity factor Z_e hereafter reflectivity, composites at 2.5-km altitude overlaid with the 700-hPa kinematic frontogenesis field from the Rapid Refresh (RAP; Benjamin et al. 2016) analysis show the hourly evolution of the comma head from 1400 to 1700 UTC as the two aircraft sampled the storm (Figs. 3a,c,d,e). The comma head exhibited a broad mesoscale region of higher Z_e that was oriented linearly from southwest to northeast. The region of higher Z_e did not fit the Novak et al. (2008) or Ganetis et al. (2018) definitions of mesoscale snowbands. For simplicity, we will refer to this linear region of higher Z_e as a band. The band axis was collocated with the axis of maximum frontogenesis at 700 hPa during all periods (white dashed line, Fig. 3). An abrupt gradient in the value of the WSR-88D correlation coefficient, determined by visual inspection, marked the location of the rain–snow line at 2.5 km along the warm side of the comma head (black dashed line, Figs. 3b,f). A second region of higher Z_e appeared along the warm side of the correlation coefficient gradient and coincided with the location of the radar bright band associated with melting ice particles at 2.5 km (Figs. 3a,c,d).

Figures 4a–f show vertical cross sections of thermodynamic and kinematic variables from the Rapid Refresh model analysis valid at 1500 UTC 7 February 2020 from central Michigan to a point south of Maine over the Atlantic Ocean (dashed black line in Fig. 2) along the flight paths of the ER-2 and P-3 over New York State (red line in Fig. 2). The warm-frontal zone is denoted by the transparent red shading, and the stationary-frontal zone by the transparent blue shading in Figs. 4a–c. In Figs. 4d–f the frontal zones are outlined by dark solid lines. The thick vertical black lines bound the region sampled by the ER-2 and P-3.

The warm front extended from the surface just south of Nova Scotia upward to a weak dynamic tropopause fold (Fig. 4a) at the 7-km level over southwestern Ontario. The

warm front was identified by an enhanced horizontal and vertical gradient of potential temperature and equivalent potential temperature, as well as an axis of kinematic frontogenesis with values ranging from 0.2 to 1.2 K (100 km)^{–1} (3 h)^{–1} (Figs. 4a–c). The surface position of the stationary front was located 50 km west of Albany, New York (Fig. 1a). The front sloped upward and westward reaching a level of ~2 km over central Michigan at 1500 UTC. This front was the boundary between air circulating anticyclonically about a 1022-hPa high pressure center located south of Hudson Bay and air circulating cyclonically off the North Atlantic north of the warm front. The front was marked by a shift of the wind from a northerly to southerly component with increasing altitude, and an enhanced horizontal and vertical gradient of potential temperature and equivalent potential temperature (Figs. 4a,b,e).

The jet axis at 1500 UTC was located at 11-km elevation on the east end of the cross section and coincided with the eastern end of the ER-2 flight legs (Fig. 4c). The jet had a maximum wind speed of 97 m s^{–1} over eastern New York State. A dry-air intrusion associated with the jet extended slantwise downward toward the east from –75.25° to –68.5° longitude from the dynamic tropopause [10 km, 2 PVU (1 PVU = 10^{–6} K kg^{–1} m² s^{–1})] to 3.5 km (Fig. 4f). Note that longitudes use a mix of degrees W and negative degrees on the figures throughout this analysis.

To better understand the air mass structure across the comma head associated with the cross sections in Fig. 4, North American Model (NAM) 12-km, 48-h HYSPLIT back trajectories were plotted every 500 m for every 1° of longitude between –85° and –70° along the cross section (Fig. 5). The atmospheric kinematic and thermodynamic structure in Fig. 4 is related to the trajectories starting within the stratosphere and continuing downward to the ground.

Air parcels within and above the jet maxima were part of the subtropical jet stream and originated 48 h earlier over the subtropical North Pacific Ocean (Fig. 5f). Air beneath the jet maxima originated within the polar front jet stream 48 h earlier over the Pacific Ocean west of Washington State and British Columbia. This air traveled through the ridge present west

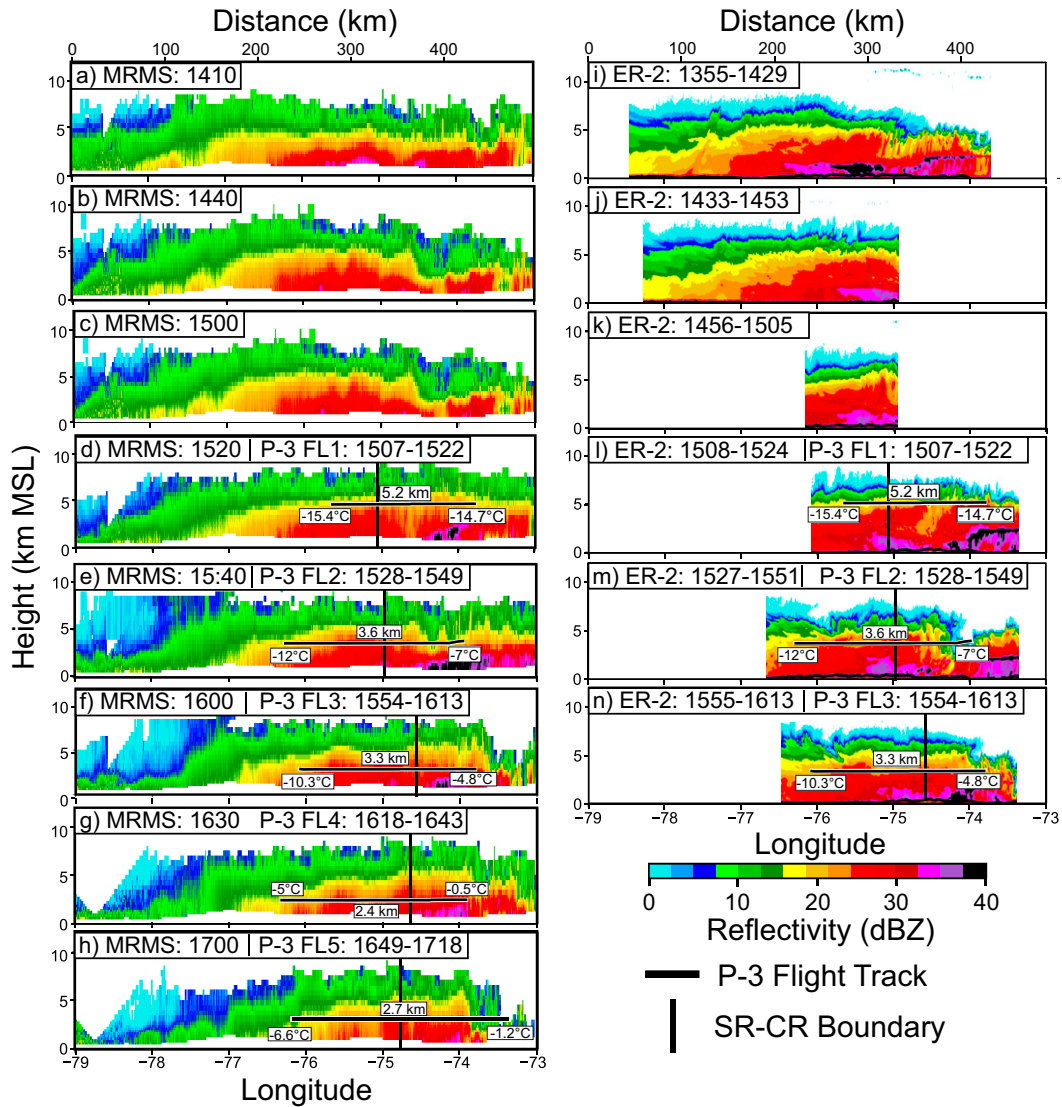


FIG. 6. (a)–(h) Cross sections of MRMS Z_e valid at times shown. (i)–(n) EXRAD Z_e cross sections. P-3 flight-level heights, temperatures, and times are overlaid over both sets of cross sections. See Table 1 for P-3 flight-leg times, temperature ranges, and ice particle growth regimes being sampled. The solid vertical black lines indicate the SR–CR boundary.

of the Rockies and then through the trough over the central United States before arriving at the cross section (Figs. 5a,e). Air within the polar jet stream had low relative humidity compared to the moist subtropical air above it (Fig. 4f). The air mass associated with the polar jet stream formed the dry-air intrusion evident in *GOES-16* satellite imagery (not shown) and influenced the stability structure on the eastern side of the cross section (see section 4).

Moist air above the warm front and below the polar jet air mass originated 48 h earlier over the Baja region and the Gulf of Mexico (Figs. 5a,d). Air parcels arriving at lower altitudes on the eastern end of the cross section had limited vertical ascent and sourced over the Gulf of Mexico while parcels with the greatest ascent, and consequently the highest relative

humidity, were sourced over the northeast Pacific at low elevations near the Baja Peninsula (Figs. 5a,d,h). Synoptic-scale ascent above the warm front was on the order of $0.3\text{--}0.5\text{ m s}^{-1}$ based on model-derived vertical motion (Fig. 4d). The air mass directly above the warm front was saturated with respect to ice and contained cloud (Fig. 4f).

Air originating beneath the stationary front was sourced 48 h earlier from air near the Canadian border north of the cross section. Air beneath the stationary front remained at low levels with most trajectories traversing eastward toward the developing low without appreciable vertical motions (Figs. 5a,b,h). Air between the two frontal zones was also saturated with respect to ice, and originated 48 h earlier over the U.S. Great Plains and the Rocky Mountains,

again without appreciable ascent over the previous 48 h (Figs. 5a,c,h).

3. IMPACTS aircraft data

The ER-2 aircraft sampled the storm between 1355 and 1613 UTC and completed six total flight legs at an altitude of approximately 20 km. The ER-2 carried three radars, the ER-2 X-band Doppler Radar (EXRAD; 9.6 GHz; Walker McLinden et al. 2021a) with a conical/cross-track scanning beam and a fixed nadir beam, the High-Altitude Imaging nadir pointing Wind and Rain Airborne Profiler (HIWRAP; Ku: 13.9 GHz; Ka: 35.6 GHz; Li et al. 2008), and the nadir pointing W-band Cloud Radar System (CRS; 94 GHz; Walker McLinden et al. 2021b). This analysis examines the horizontal variability of cloud substructures and circulations using the EXRAD fixed nadir beam equivalent reflectivity factor Z_e in order to take advantage of reduced attenuation, and the CRS vertical radial velocity V_r due to its smaller beamwidth and higher sensitivity (Walker McLinden et al. 2021a). The EXRAD beamwidth is 3.3° with a footprint of 1.2 km at the surface when the aircraft is flying at 20 km. The CRS beamwidth is 0.46° with a footprint of 0.16 km at the surface from the same altitude.

The P-3 aircraft sampled the storm between 1507 and 1718 UTC, completing seven total flight legs. On flight legs 6 and 7, the reflectivity in the upper part of the cloud had weakened substantially. Elevated convection, and its impact on precipitation, had ceased by the time the fifth leg was completed and the P-3 was only sampling the rapidly weakening stratiform region of the comma head at higher altitudes. Therefore, flight legs 6 and 7 were not included in the analysis in this paper. This analysis considers the first five P-3 flight legs [referred to as flight legs 1–5 (FL1–5) in Table 1]. The P-3 flight legs were completed at altitudes between 2 and 6 km, and at temperatures between 0° and -27°C and are shown in subsequent figures from highest to lowest altitude. Both aircraft flew a fixed flight track over central New York from longitudes of approximately -73.5° to -76.5° , with latitudes varying between 42.9° and 43.1° . Three flight legs between the ER-2 and P-3 were coordinated, followed by additional P-3 flight legs when the ER-2 returned to base.

Figures 6a–h show vertical Multi-Radar Multi-Sensor (MRMS; Smith et al. 2016) cross sections of WSR-88D Z_e during all ER-2 and P-3 flight legs together with EXRAD Z_e (Figs. 6i–n) along the same cross section when available. The P-3 arrived onsite after the ER-2 had completed three flight legs (Figs. 6l–n). The height, location, and temperatures at which the P-3 was sampling are noted along each MRMS and EXRAD cross section. The ER-2 departed at 1613 UTC, and the P-3 continued to sample through 1820 UTC. The vertical cross sections show the storm weakening from the west with time especially along later P-3 flight legs. The mesoscale snowband was visible in EXRAD Z_e cross sections (at 2.5 km where Z_e was > 32.5 dBZ) but was too fine scale and/or low to be retrieved by the MRMS resampling algorithm. The vertically stacked flight legs of the P-3 allowed for the sampling

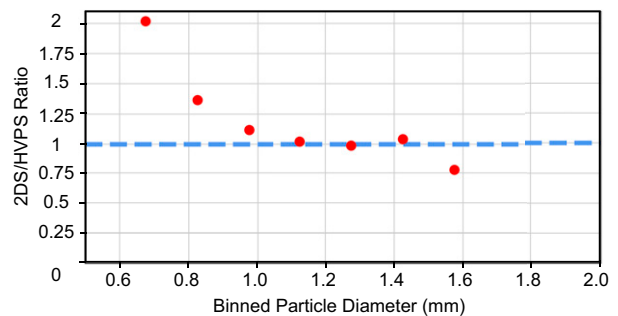


FIG. 7. Mean ratio of the 2DS and HVPS concentrations (maximum diameters $D > 100 \mu\text{m}$) normalized by bin width.

of different particle growth layers and a vertical profile of particle growth in the comma head of the 7 February 2020 snowstorm.

The P-3 aircraft was equipped with a full suite of microphysics instrumentation, including a Cloud Droplet Probe (CDP; Lance et al. 2010, 2012), a Two-Dimensional Stereo probe (2DS; Lawson et al. 2006), and High-Volume Precipitation Spectrometers (HVPS-3A and HVPS-3B; Lawson et al. 1993, 1998) for particle size information. The HVPS-3A (hereafter referred to as HVPS) was mounted to the P-3 vertically (its orientation consistent with the channel used herein with the 2DS). A Particle Habit Imaging and Polar Scattering Probe (PHIPS; Abdelmonem et al. 2016; Schnaiter et al. 2018) was used for particle imagery and the Rosemount Icing Detector (RICE; Baumgardner and Rodi 1989) for supercooled water detection. Data from the CDP were used for particles between 2 and $50 \mu\text{m}$, the 2DS for particles between 100 and $1400 \mu\text{m}$ (1.4 mm), and the HVPS for particles $> 1400 \mu\text{m}$ (1.4 mm). The size ranges used for the 2DS and HVPS probes were determined as follows: 1) A lower threshold ($100 \mu\text{m}$) for the 2DS was chosen in accordance with previous studies to minimize uncertainty in the depth of field (e.g., Lawson et al. 2006) and to remove potentially shattered artifacts (e.g., Korolev et al. 2011; Jackson and McFarquhar 2014). 2) An upper threshold ($1400 \mu\text{m}$, or 1.4 mm) was selected as the 2DS-HVPS cutoff point. The 1.4-mm threshold was selected because the concentrations from the 2DS and HVPS most consistently overlapped at this size (Fig. 7), even though this size is larger than the approximately 1-mm threshold that has been used in several prior studies (e.g., Hu et al. 2021).

Two-Dimensional Stereo and HVPS probe data were processed using the University of Illinois/Oklahoma Optical Array Probe Processing Software (UIOOPS; McFarquhar et al. 2018). Using UIOOPS, several steps were taken to ensure the quality of the data. A time-dependent threshold, calculated for every 25 000 particles, was used to remove shattered artifacts from the 2DS data following the approaches of Field et al. (2006) and Stechman et al. (2020). Following the removal of shattered artifacts, an additional processing technique was applied to estimate particle size for particles that were not entirely within the 2D sensing area, as outlined in Heymsfield and Parrish (1978). Finally, the size of each

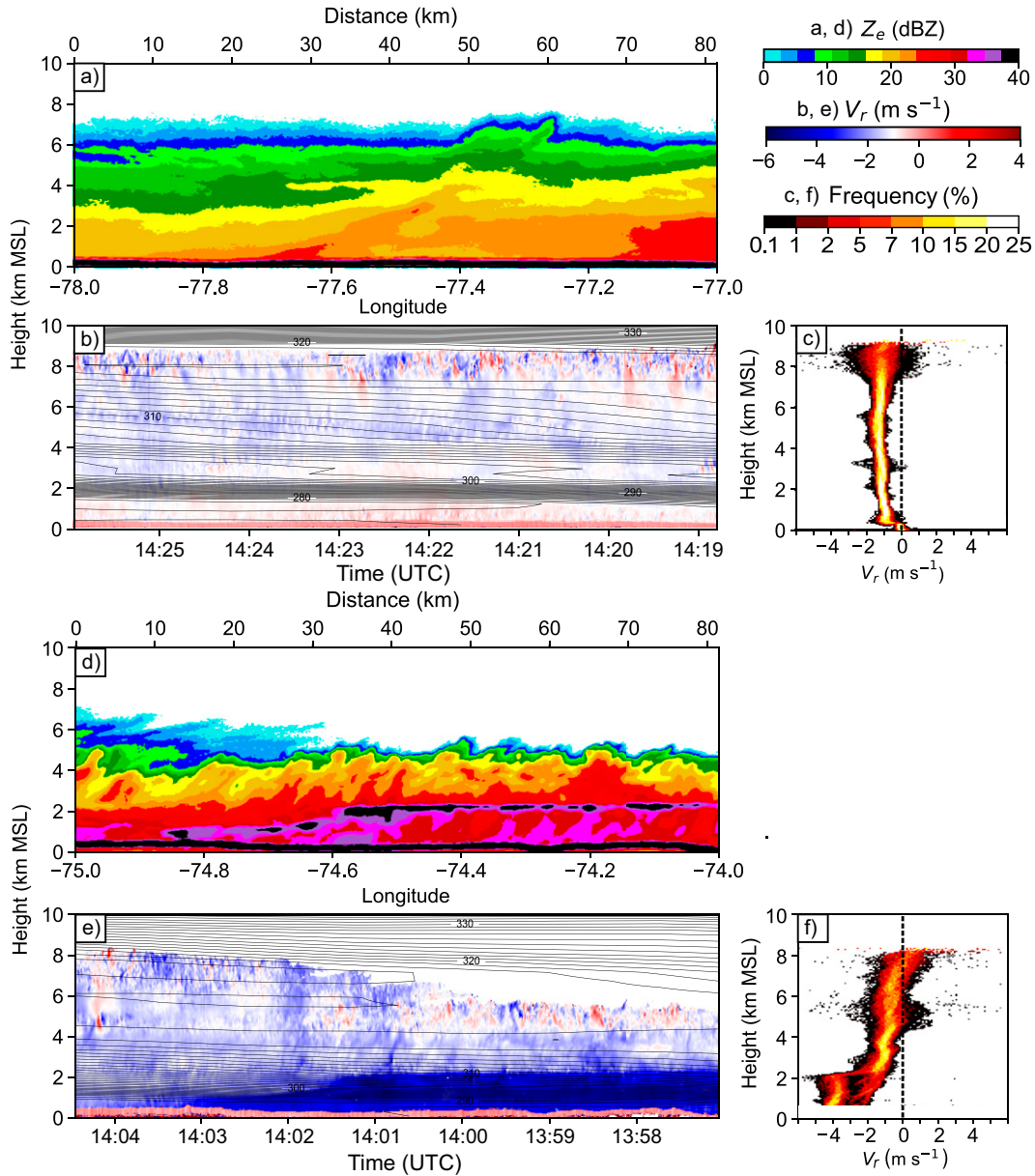


FIG. 8. Expanded segments of FL1 from the (a),(b) SR and (d),(e) CR. (a) EXRAD Z_e valid between 1418:47 and 1425:56 UTC 7 Feb 2020 in the SR. (b) CRS V_r (m s^{-1}) from flight leg 1 overlaid with θ_e (K) in the SR. (c) Contoured frequency by altitude diagram (CFAD) of CRS V_r , binned every 100 m in altitude and 0.1 m s^{-1} for the data in (b). (d) EXRAD Z_e valid between 1357:04 and 1404:26 UTC 7 Feb 2020 in the CR. (e) CRS V_r (m s^{-1}) overlaid with θ_e (K) in the CR. (f) CFAD of CRS V_r , binned every 100 m in altitude and 0.1 m s^{-1} for the data in (e).

particle was determined as the diameter of the minimum enclosing circle, and bulk microphysical characteristics were calculated at 1-Hz intervals. The 2DS experienced overloads (McFarquhar et al. 2017) where particle images were lost. When this occurred, there was a dead period when no data were recorded. Although the 2DS tracks dead time so that the sample volume can be corrected during overload periods, it is uncertain how reliable size distributions and the calculation of total number concentration are for time periods with

large dead time. In this study, all 1-s periods with a dead time greater than 0.7 s were removed from subsequent analysis. Further, periods with dead times greater than 0.2 s were flagged and are denoted in the 2DS time series appearing later in the paper as calculated concentrations are more uncertain in these regions. Large dead times primarily occurred during the first P-3 flight leg. If a more stringent dead time than 0.7 s was chosen for inclusion, there would be a bias away from times with higher concentrations (see appendix).

TABLE 2. Location and time of the stratiform–convective boundary based on PHIPS stereo images. Periods of the westernmost rain–snow transition observed during P-3 flight legs are also noted.

Flight leg	SR–CR boundary microphysics lon (°)	SR–CR boundary microphysics time (UTC)	Westernmost rain–snow boundary lon (°)	Westernmost rain–snow time
1	−75.06	1512:02	—	—
2	−74.97	1537:18	—	—
3	−74.64	1606:25	—	—
5	−74.67	1703:16	−73.58	1713:48
4	−74.86	1628:18	−73.92	1618:26

In addition to the quantitative information provided by the 2DS and HVPS probes, PHIPS stereo imagery was manually classified according to particle habit types identified in [Bailey and Hallett \(2009\)](#). Information about particle characteristics, particle growth, riming, dendritic growth, and particle habit were manually recorded and quantified for FL 1–3 using the same approach as in [Waitz et al. \(2022\)](#). The manual classification was performed by three people independently from each other. In total, 9134 stereo-image pairs were visually inspected, from which 3414 were assigned a habit classification. Images that were not given a habit assignment were shattering events where no identification of the original particle was possible. The absolute uncertainty in the given particle fraction is around $\pm 5\%$.

Five microphysical quantities were analyzed: 1) total number concentration (N_t), 2) ice water content (IWC), 3) supercooled liquid water (SLW) content, 4) composite ice particle size distributions, and 5) PHIPS stereo images to determine particle habit and characteristics. Values of N_t were calculated by summing the number concentration within each bin of the 2DS probe (N_{2DS} , particle sizes with maximum diameters (D) $100 \mu\text{m} < D < 1.4 \text{ mm}$) and the number concentration within each bin of the HVPS probe (N_{HVPS} , particles sizes $D > 1.4 \text{ mm}$). Composite particle size distributions in the stratiform and convective regions of the storm were developed from the 2DS and HVPS measurements. Total ice water content was calculated using mass–area relationships following [Baker and Lawson \(2006\)](#). Mass may be underestimated for particles that touch the edge of the photodiode array since the particle area could not be reconstructed. This mass underestimation is more likely for particles approaching 1.4 mm as the 2DS field of view is only 1.28 mm. The CDP and RICE probes were used together to detect SLW when temperatures were lower than -7°C . The CDP can be triggered by both cloud droplets and ice particles. Periods with CDP concentrations $> 10 \text{ cm}^{-3}$ or voltage changes of at least 2 Hz were identified as periods with SLW present (e.g., [Hobbs and Rangno 1998](#); [Cober et al. 2001](#); [Lance et al. 2010](#); [Um et al. 2018](#); [Finlon et al. 2019](#); [Wang et al. 2020](#)). At temperatures greater than -7°C , the RICE probe data become unreliable and only the CDP concentration criteria were used to identify SLW regions. Cloud liquid water measurements were made at a rate of 1 Hz.

Several distinct temperature layers were observed by the P-3, which correspond to the ice particle growth regimes identified by [Bailey and Hallett \(2009\)](#) as a function of

temperature and supersaturation. Using the Bailey and Hallett criteria, temperature (T) layers were defined as follows: 1) the polycrystalline growth layer (PCGL; $T < -18^\circ\text{C}$), 2) the dendritic growth layer (DGL; $-18^\circ \leq T < -12^\circ\text{C}$), 3) the plate growth layer (PGL; $-12^\circ \leq T < -8^\circ\text{C}$), and 4) the needle growth layer (NGL; $-8^\circ \leq T < -3^\circ\text{C}$). An additional layer, the enhanced aggregation layer (EAL), was defined between -3° and 0°C . Note that although particle habits are established in these layers, particles with these habits can be observed at warmer temperatures as particles fall through the cloud.

The variability and magnitude of N_t , IWC, and SLW are quantitatively analyzed using box-and-whisker plots that show the minimum and maximum values (N_{\min} and N_{\max}), 25th- and 75th-percentile values (N_{25} and N_{75}), and median values (N_{median}), where each data point represents a 1-Hz sample, or for the CDP, 1 Hz SLW content integrated from the droplet size distributions. Particle size distributions were developed for the stratiform and convective regions on each flight leg as discussed below. N_{2DS} and N_{HVPS} were also calculated within those regions. PHIPS stereo images shown are the most representative particle habits within these regions.

Vapor deposition was inferred by examining the existence of faceted crystals in the PHIPS stereo images and whether they were consistent with temperature regimes defined in [Bailey and Hallett \(2009\)](#), or consistent with temperatures above the altitude they were observed (implying that the particles fell from aloft). Increases in IWC between layers provided quantitative evidence for vapor depositional growth. Particle growth consistent with aggregation was inferred by decreases in N_t and N_{2DS} that were accompanied by increases in N_{HVPS} between layers. PHIPS stereo images were used to qualitatively confirm aggregation. Particle growth by riming was inferred by the presence of frozen cloud droplets attached to ice particles in PHIPS stereo images. Some [Bailey and Hallett \(2009\)](#) defined particle growth layers were sampled on two or more flight legs; when this occurred, microphysical quantities from each flight leg will be presented.

To identify particle growth mechanisms consistent with observations through the depth of the cloud requires the assumption that a steady state exists during the 3-h sampling time of the flight legs. Although trends in the microphysical data were generally consistent with particle growth mechanisms expected in various layers, the observations were not

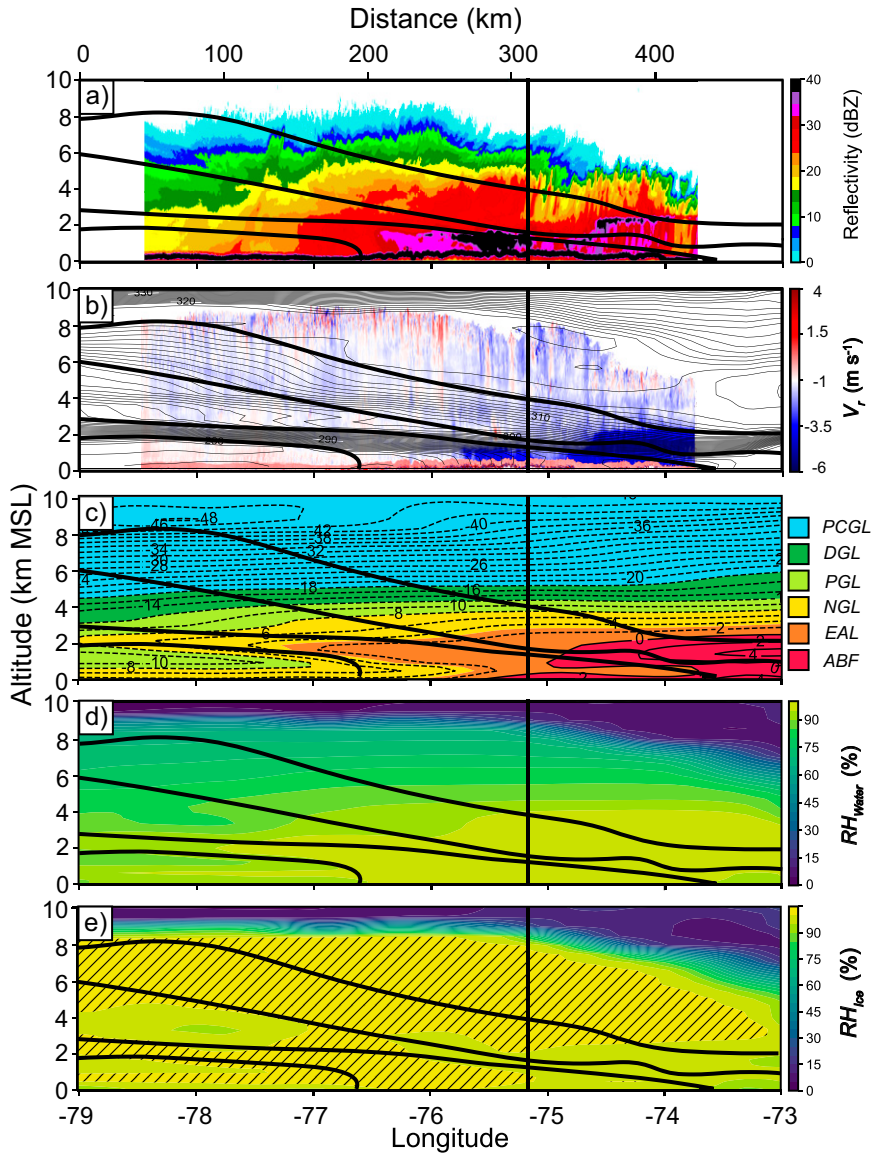


FIG. 9. (a) ER-2 EXRAD Z_e cross section from 1355 to 1429 UTC 7 Feb 2020. (b) ER-2 CRS vertical V_r (m s^{-1}) overlaid with θ_e (K) from RAP analysis valid at 1500 UTC. (c) Particle growth layers overlaid with temperature from RAP analysis at 1500 UTC ($^{\circ}\text{C}$) (Bailey and Hallett 2009). Particle growth layers include the polycrystalline growth layer (PCGL) in blue, the dendritic growth layer (DGL) in green, the plate growth layer (PGL) in lime green, the needle growth layer (NGL) in yellow, the enhanced aggregation layer (EAL) in orange, and the above freezing layer (ABF) in red. (d) Relative humidity with respect to water (RH_{water}). (e) Relative humidity with respect to ice (RH_{ice}). Hatched regions denote $\text{RH}_{\text{ice}} > 100\%$. On all cross sections the stationary- and warm-frontal zones are outlined by black lines. Solid vertical lines on all panels indicate the boundary between the SR and CR estimated from Z_e and V_r . The P-3 had not yet arrived, and microphysical data were not available on this flight leg.

obtained in a Lagrangian framework or in a steady-state cloud system, especially given that the component of the wind normal to the cross section was large (Fig. 4e). Winds beneath the stationary front were northerly at $10\text{--}13 \text{ m s}^{-1}$, while winds above the warm front were southerly at $20\text{--}50 \text{ m s}^{-1}$.

The entire weather system moved northward during the sampling period, with MRMS radar echoes in both the eastern (convective) region and western (stratiform) region weakening with time, particularly after FL5 of the P-3. For this reason, analyses herein are limited to the first five P-3

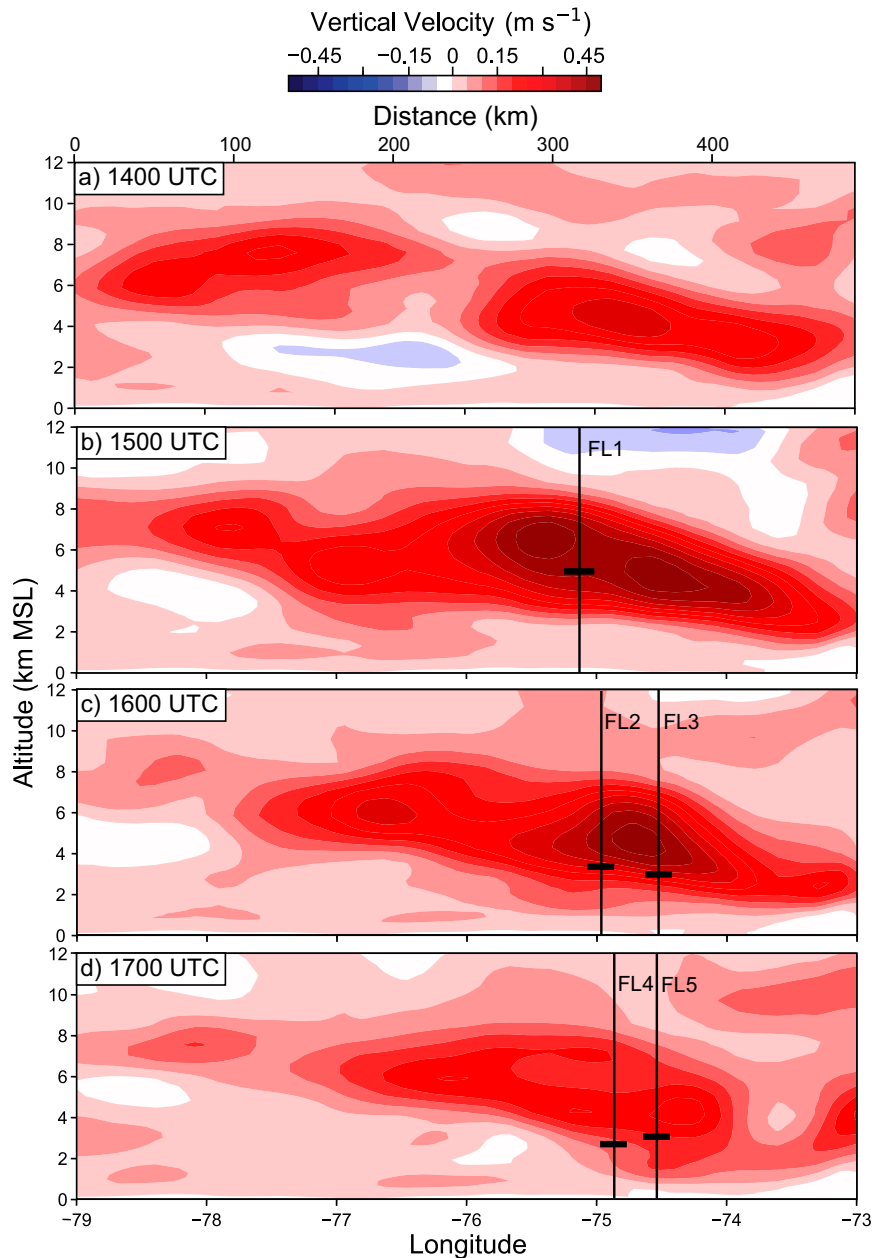


FIG. 10. Model w from RAP analysis valid at (a) 1400, (b) 1500, (c) 1600, and (d) 1700 UTC 7 Feb 2020. Solid vertical lines delineate the boundary between the stratiform region (to the left) and convective region (to the right) determined using microphysics data. The horizontal line indicates the flight height along a given research flight.

flight legs. The results shown in section 5 should be interpreted with these caveats in mind.

4. Stability and moisture characteristics

For the purpose of microphysical analysis, airborne measurements of Z_e and V_r collected by the ER-2 aircraft, together with thermodynamic data from the RAP analysis, were used to divide the sampling cross section within the comma head

into two distinct regions. Figure 8 shows shorter Z_e and V_r cross sections of ER-2 FL1 that were representative of these two regions. To the west, the comma head was characterized by a deep stratiform region (SR) with Z_e increasing eastward and with depth beneath cloud top (Fig. 8a). Except near radar echo top, the CRS V_r showed little variation with depth beneath cloud top, with a median value ranging from -1.2 to -0.9 m s^{-1} between 2 and 7.5 km, typical terminal velocity values for unrimed ice particles falling from high altitudes to the ground (Figs. 8b,c)

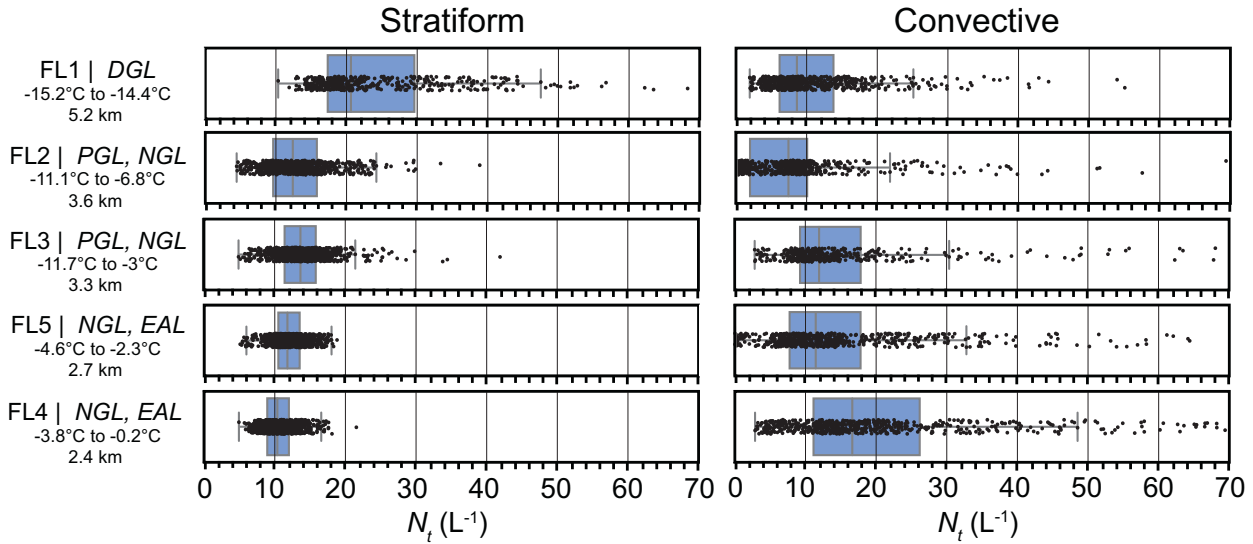


FIG. 11. Box-and-whiskers plot of N_t (L^{-1}) for (left) the stratiform region and (right) the convective region for all 1-Hz samples with dead time ≤ 0.7 s. Boxplots have temperatures organized from (top) lowest temperature to (bottom) highest temperature, specifically, DGL, PGL, NGL, and EAL. Boxes represent the 25th, 50th, and 75th percentiles. Whiskers represent the mean ± 1.5 times the interquartile range. Times of each flight leg can be found in Table 1 and percentiles in Table 3.

(e.g., Rosenow et al. 2014; Grasmick and Geerts 2020). Below the cloud-top region, none of the values exceeded 0 m s^{-1} . The cloud top in the SR was capped by generating cells which had a depth of 1 km with a median V_r of 0.75 m s^{-1} and extreme values of V_r approaching $+1 \text{ m s}^{-1}$ (Fig. 8c). To the east, an elevated convective region (CR) was present within the comma head, with Z_e in the layer between 3 km and echo top characterized by reflectivity towers east of -75.2° longitude (Fig. 8d). The layer between 5 and 7 km within the CR was weakly potentially unstable, and V_r within this region had median values ranging from -0.75 to -0.4 m s^{-1} and extreme values approaching $+2 \text{ m s}^{-1}$ (Figs. 8e,f). Updrafts extending to cloud top had median V_r of 0.25 m s^{-1} with extreme values again approaching $+2 \text{ m s}^{-1}$. In the CR, the median V_r decreased with depth beneath cloud top to values near -2 to -1.5 m s^{-1} just above the melting layer, which was located at

the 3-km level on the east side of the CR. The melting layer sloped downward to the surface west of -74.6° longitude.

The position of the SR–CR boundary was determined qualitatively from the EXRAD radar data and by a distinct change in particle habits determined using PHIPS stereo imagery. This boundary was evident on all five P-3 flight legs. Times and locations used to separate the SR from the CR can be found below in Table 2. In section 5 the microphysical boundary is used to delineate processes within the two regions.

The SR was characterized by a stable vertical profile (Fig. 9b) with synoptic-scale vertical motion above the warm-frontal zone of $0.1\text{--}0.3 \text{ m s}^{-1}$ (Fig. 10), lower temperatures (Fig. 9c), intrusion of unsaturated air in the midlevels on the western side of the cross section (Figs. 9d,e), and an overall weakening trend

TABLE 3. Measurements of total number concentration (L^{-1}) for the minimum (N_{\min}), 25th-percentile (N_{25}), 50th-percentile (N_{50}), 75th-percentile (N_{75}), and maximum (N_{\max}) values in the stratiform and convective regions corresponding to Fig. 11. For flight levels where more than 20% of the 1-s time periods have dead times (dt) > 0.2 s, separate statistics on N_t are provided using a more conservative dead-time threshold (≤ 0.2 s).

Flight leg	Stratiform region					Convective region						
	Particle growth layer	N_{\min}	N_{25}	N_{50}	N_{75}	N_{\max}	Particle growth layer	N_{\min}	N_{25}	N_{50}	N_{75}	N_{\max}
1(dt ≤ 0.2 s)	DGL	10.3	15.9	17.6	19.4	27.5	DGL	1.9	5.3	7.6	10.2	33.4
1(dt ≤ 0.7 s)	DGL	10.3	17.3	20.6	29.6	99.6	DGL	1.9	6.2	8.6	13.8	55.0
2(dt ≤ 0.2 s)	PGL	4.5	8.8	10.4	12.4	18.8	PGL, NGL	0.1	2.0	7.5	10.1	57.5
2(dt ≤ 0.7 s)	PGL	4.5	9.6	12.4	15.8	38.9	PGL, NGL	0.1	2.1	7.5	10.2	69.4
3(dt ≤ 0.2 s)	PGL	5.0	11.2	13.2	15.2	21.2	PGL, NGL	2.8	8.9	10.9	15.4	172.3
3(dt ≤ 0.7 s)	PGL	5.0	11.5	13.8	15.9	42.0	PGL, NGL	2.8	9.3	11.9	17.8	174.1
5	NGL	5.0	10.5	11.8	13.5	18.8	NGL, EAL	0.1	7.8	11.5	17.8	121.7
4	NGL	5.0	9.0	10.4	12.1	21.6	NGL, EAL	3.0	11.2	16.7	26.2	140.5

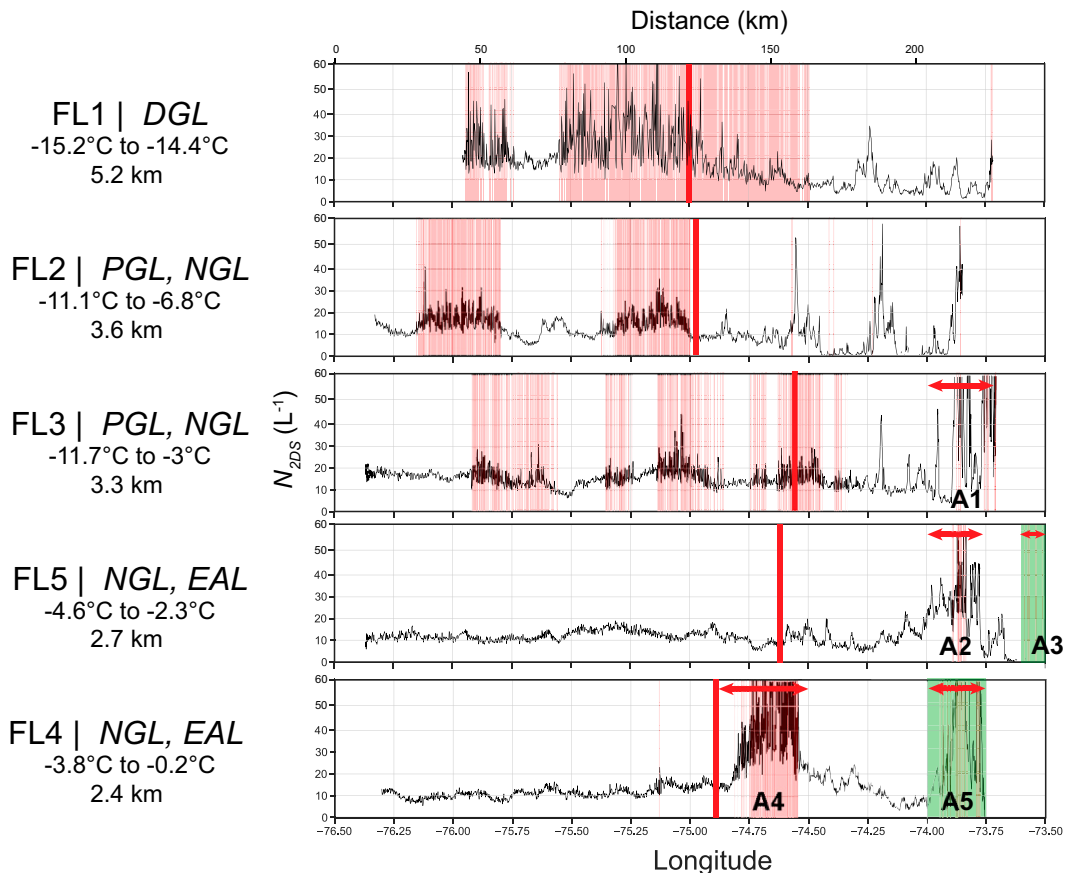


FIG. 12. $N_{2DS} (L^{-1})$ for each flight leg as a function of longitude for all 1-Hz samples with dead time ≤ 0.7 s. The red solid line along each flight leg indicates the microphysics boundary between the stratiform and convective regions. Red arrows are subsets of microphysical data that will be shown in Fig. 21. Green shaded areas are regions where raindrops were observed. Pink shaded regions are periods of 2DS dead time > 0.2 s.

in precipitation during the sampling period with WSR-88D reflectivity decreasing from ~ 20 dBZ at 1500 UTC to ~ 10 dBZ by 1800 UTC (Figs. 6i,j). Within the SR, relative humidity with respect to ice (RH_{ice}) exceeded 100% above the warm front and below the stationary front but decreased beneath 100% between 2 and 4 km (Fig. 9e). No air was saturated with respect to water within the SR based on the RAP analysis (Fig. 9d). With only weak, nonconvective vertical motions below cloud top observed with the CRS radar V_r , air within the SR would have rarely reached water saturation in the natural cloud (Fig. 9b). Precipitation reached the ground as snow within the SR, except possibly within the mesoscale snowband (Fig. 9c). There, between the surface and 1-km altitude, V_r decreased from ~ -1 to -4 $m s^{-1}$, characteristic of ice particles melting into raindrops (Fig. 9b). No direct observations were available at the surface beneath the band to determine whether precipitation at the ground consisted of wet snowflakes or rain, but the higher reflectivities associated with the band were clearly influenced by melting (Fig. 9a).

The CR was characterized by higher temperatures, higher ice supersaturations relative to the SR (Figs. 9c,e), and synoptic-scale vertical motions above the warm-frontal zone

of 0.2 – 0.5 $m s^{-1}$ (Fig. 10). The primary features of the CR were 2–2.5-km-deep sloped reflectivity plumes descending beneath elevated convection (Figs. 9a,c). The location of these convective vertical motions coincided with a layer of weak potential instability along the interface of the moist air mass over the warm front and drier air associated with the polar front jet (Figs. 4f, 5a, 9e). Based on the presence of SLW within convection sampled by the P-3 (see next section), the convective vertical motions were sufficient for the rising air to exceed water saturation.

5. Microphysical characteristics

a. Stratiform region

As evident in Fig. 6, the radar reflectivity within the SR weakened with time, particularly on the west side of the cross section. Flight legs 1–4 (FL1–4) sampled the DGL, PGL, and NGL progressively downward earlier in the storm, with FL5 higher in altitude than FL4, but also in the NGL.

FL1 sampled the DGL at an altitude of 5.2 km (-15.9° to -15.0°) in the SR. Values of N_i ranged from 10.3 to 99.6 L^{-1}

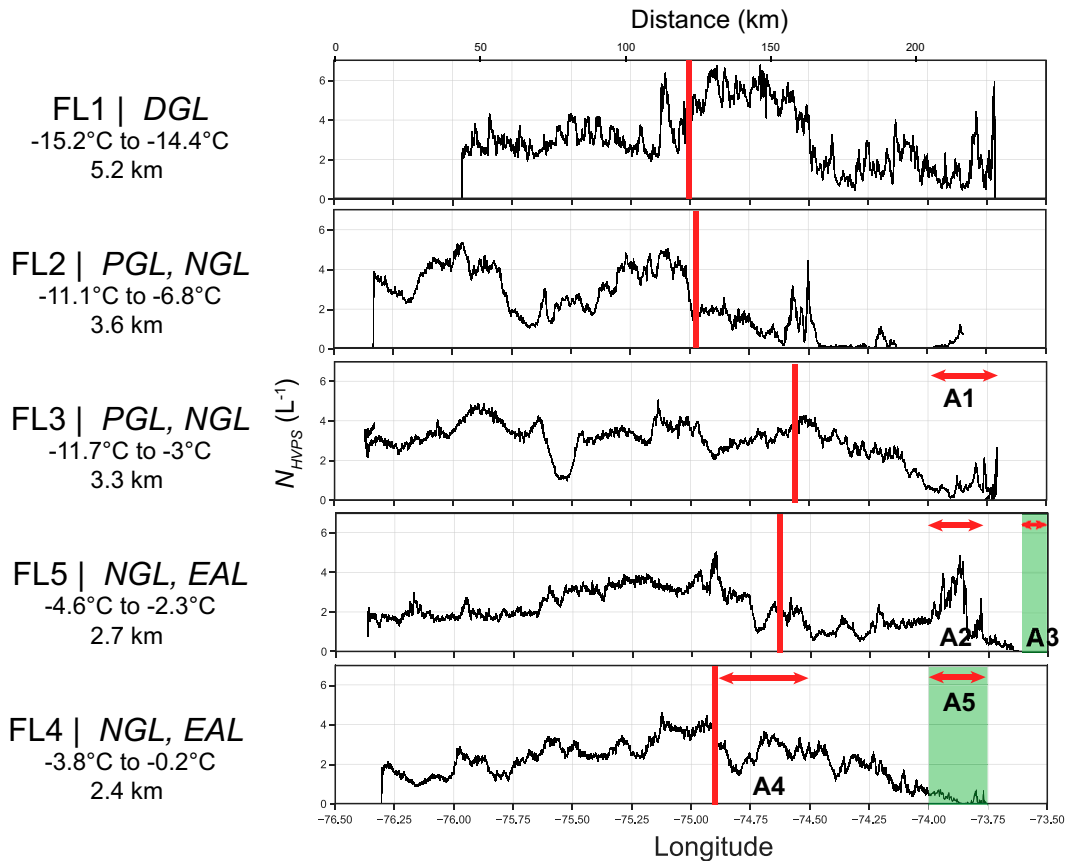


FIG. 13. As in Fig. 12, except $N_{HVPS} (L^{-1})$ is shown.

with $N_{median} = 20.6 L^{-1}$ (Fig. 11, Table 3) for periods with dead time ≤ 0.7 s and from 10.3 to $27.5 L^{-1}$ with $N_{median} = 17.6 L^{-1}$ for periods with dead time ≤ 0.2 s (Table 3). N_{2DS} and N_{HVPS} varied little relative to the CR across the SR at this altitude (Figs. 12, 13). The particle size distribution (PSD) had mean $N_{2DS} = 21.5 L^{-1}$ ($15.0 L^{-1}$ for periods with dead time ≤ 0.2 s) and had mean $N_{HVPS} = 3.0 L^{-1}$ (Fig. 14, Table 4). Limited SLW was present across the SR in the DGL, consistent with the air being unsaturated with respect to water and dendritic particle formation and growth not occurring (Figs. 15–17). Particle habit analysis using PHIPS stereo imagery showed primarily side planes (83.5% of particles), other polycrystalline habits (9.7% of particles) and single platelike particles (3% of particles) (Figs. 18, 19, Table 5) consistent with the fall of particles from above the flight altitude into the DGL from the PCGL, rather than formation in the DGL. Of the PHIPS analyzed particles, 96.1% were unrimed in the SR on FL1. The IWC of the particles in the DGL ranged from 0.5 to $1.7 g m^{-3}$, with $IWC_{median} = 0.8 g m^{-3}$ (Fig. 20, Table 6).

FL2 sampled the PGL (-12.2° to $-8.3^{\circ}C$) at an altitude of 3.6 km and FL3 sampled the PGL and colder temperatures of the NGL (-12.8° to $-7.3^{\circ}C$) at an altitude of 3.3 km. N_i ranged from 4.5 to $38.9 L^{-1}$ with $N_{median} = 12.4 L^{-1}$ on FL2 (from 4.5 to $18.8 L^{-1}$ with $N_{median} = 10.4 L^{-1}$ for dead time ≤ 0.2 s) and from

5.0 to $42.0 L^{-1}$ with $N_{median} = 13.8 L^{-1}$ on FL3 (from 5.0 to $21.2 L^{-1}$ with $N_{median} = 13.2 L^{-1}$ for dead time ≤ 0.2 s) (Fig. 11, Table 3), concentrations comparable to those sampled in the DGL. Again, N_{2DS} and N_{HVPS} varied little relative to the CR across the SR at these altitudes (Figs. 12, 13). Averages of $N_{2DS} = 9.9 L^{-1}$ ($7.9 L^{-1}$ for dead time ≤ 0.2 s) and $N_{HVPS} = 3.2 L^{-1}$ for FL2 and $N_{2DS} = 10.8 L^{-1}$ ($10.0 L^{-1}$ for dead time ≤ 0.2 s) and $N_{HVPS} = 3.2 L^{-1}$ for FL3 (Fig. 14, Table 4) were observed. Again, there was no SLW observed on both flight legs (Figs. 15–17), and PHIPS stereo-imagery analysis showed side planes (76.8%–82.2% of particles), polycrystalline habits (6.3%–7.2% of particles) and single platelike particles (2.4%–2.9% of particles) (Figs. 18, 19, Table 5). On FL2–3 over 90% of PHIPS analyzed particles were unrimed and any riming was very light. Capped columns and plate-column mixes were also observed (4.6%–6.2% of particles). The IWC of the particles in the PGL on FL2 ranged from 0.4 to $2.9 g m^{-3}$, with $IWC_{median} = 1.1 g m^{-3}$, and on FL3 ranged from 0.6 to $1.7 g m^{-3}$, with $IWC_{median} = 1.1 g m^{-3}$ (Fig. 20, Table 6). These data together imply that most particles fell from aloft and continued to grow by vapor deposition as they fell through the PGL and upper NGL, with few new particles, such as plate-column mixes, forming in situ.

FL4 and FL5 sampled the NGL at altitudes of 2.4 km (-5.0° to $-2.8^{\circ}C$) and 2.7 km (-6.6° to $-4.5^{\circ}C$). Again, there

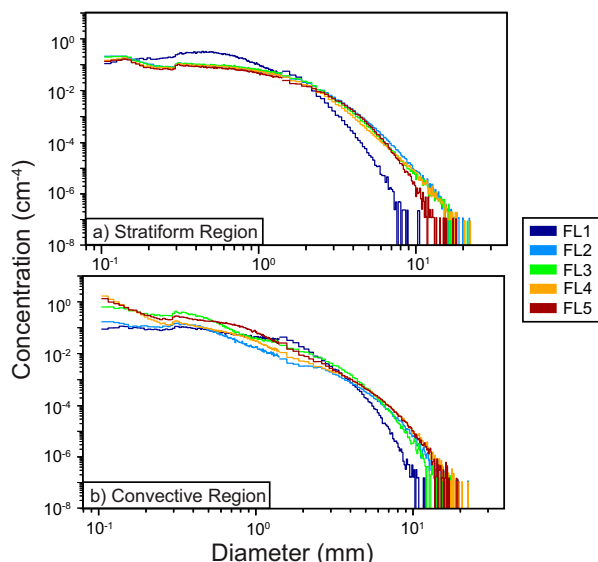


FIG. 14. Representative particle size distributions averaged separately over the (a) SR and (b) CR for each flight leg for the 2DS and HVPS with 2DS dead time ≤ 0.7 s. Flight-leg times can be found in Table 1 and the boundaries between the CR and SR can be found in Table 2. Mean 2DS and HVPS N_i for each flight leg can be found in Table 4. At smaller sizes FL2–5 have similar concentrations and overlap in (a).

was little variation along the track in N_{2DS} or N_{HVPS} at these altitudes (Figs. 12, 13). For example, N_i ranged from 5.0 to 21.6 L^{-1} with $N_{median} = 10.4 L^{-1}$ on FL4 and from 5.0 to 18.8 L^{-1} with $N_{median} = 11.8 L^{-1}$ on FL5 (Fig. 11, Table 3), concentrations similar to that within the PGL. Since dead times were minimal on FL4 and FL5, there were few potential periods with high concentrations that would be excluded using a more conservative dead-time threshold. The PSDs had $N_{2DS} = 8.3 L^{-1}$ and $N_{HVPS} = 2.5 L^{-1}$ for FL4 and $N_{2DS} = 9.4 L^{-1}$ and $N_{HVPS} = 2.6 L^{-1}$ for FL5 (Fig. 14, Table 4). There was limited SLW on either flight leg (Figs. 15 and 17), and PHIPS stereo imagery again showed that the dominant particle habits were side planes and platelike particles with a few plates and capped columns. The IWC of the particles in the NGL on FL4 ranged from 0.2 to 2.1 $g m^{-3}$, with

$IWC_{median} = 1.0 g m^{-3}$ and on FL5 from 0.3 to 1.8 $g m^{-3}$, with $IWC_{median} = 0.9 g m^{-3}$ (Fig. 20, Table 6).

A comparison of backscatter coefficient and depolarization ratio from the cloud physics lidar revealed that cloud top within the SR was dominated by ice. Based on the lidar returns at cloud top, no supercooled water was present. The cloud top was colder than $-40^\circ C$ across most of the SR meaning side planes likely formed as a result of heterogeneous freezing on aerosol at temperatures colder than $-40^\circ C$. Based on aircraft in situ measurements, and habit analysis, there was very limited supercooled liquid water if any present within the SR beneath cloud top and growth by accretion was relatively rare. There was no systematic increase in N_{HVPS} with depth between the aircraft flight levels (Fig. 13) implying that growth by aggregation was also limited. In situ measurements in the SR are consistent with the formation of side planes and platelike particles forming in the upper part of the cloud above the highest flight level and growing by vapor deposition through the depth of the cloud.

b. Convective region

FL1–4 sampled the convective region descending on each subsequent flight leg through the DGL, PGL, NGL, and EAL, with FL2–4 sampling more than one growth layer because the isotherms sloped upward toward the east. FL5 sampled the NGL and EAL.

FL1 sampled the DGL at an altitude of 5.2 km (-15.6° to $-13.9^\circ C$) in the CR. N_i ranged from 1.9 to 55.0 L^{-1} with $N_{median} = 8.6 L^{-1}$ (Fig. 11, Table 3) for periods with dead time ≤ 0.7 s and from 1.9 to 33.4 L^{-1} with $N_{median} = 7.6 L^{-1}$ for periods with dead time ≤ 0.2 s (Table 3). There were isolated peaks in N_{2DS} up to 30–60 L^{-1} along the flight leg (Fig. 12). The mean PSD across the CR had $N_{2DS} = 8.1 L^{-1}$ ($6.6 L^{-1}$ for dead time ≤ 0.2 s) and $N_{HVPS} = 2.8 L^{-1}$ (Fig. 14, Table 4). The CDP detected SLW in the DGL between -75.25° to -74.5° longitude with typical SLW values ranging from 0.01 to 0.05 $g m^{-3}$ with maximum values up to 0.15 $g m^{-3}$ (Figs. 15, 16). Droplet concentrations in SLW regions ranged from 20 to 30 cm^{-3} (Fig. 17). PHIPS stereo-imagery analysis revealed a mix of particle habits including side planes (53.0% of particles), polycrystalline (16.9% of particles) and other plates (6.9% of particles), dendrites (14.8% of

TABLE 4. Mean particle concentration measurements of N_{2DS} and N_{HVPS} corresponding to size distributions in Fig. 14 (L^{-1}). For flight levels where more than 20% of the 1-s time periods have dead times (dt) > 0.2 s, separate statistics on N_i are provided using a more conservative dead-time threshold (≤ 0.2 s).

Flight leg	Stratiform region			Convective region		
	Particle growth layer	N_{2DS}	N_{HVPS}	Particle growth layer	N_{2DS}	N_{HVPS}
1 (dt ≤ 0.2 s)	DGL	15.0	3.0	DGL	6.6	2.8
1 (dt ≤ 0.7 s)	DGL	21.5	3.0	DGL	8.1	2.8
2 (dt ≤ 0.2 s)	DGL	7.9	3.2	DGL	7.1	0.8
2 (dt ≤ 0.7 s)	DGL	9.9	3.2	DGL	7.3	0.8
3 (dt ≤ 0.2 s)	DGL	10.0	3.2	DGL	16.7	2.1
3 (dt ≤ 0.7 s)	DGL	10.8	3.2	DGL	19.8	2.1
5	NGL	9.4	2.6	NGL, EAL	15.3	1.4
4	NGL	8.3	2.5	NGL, EAL	20.9	1.7

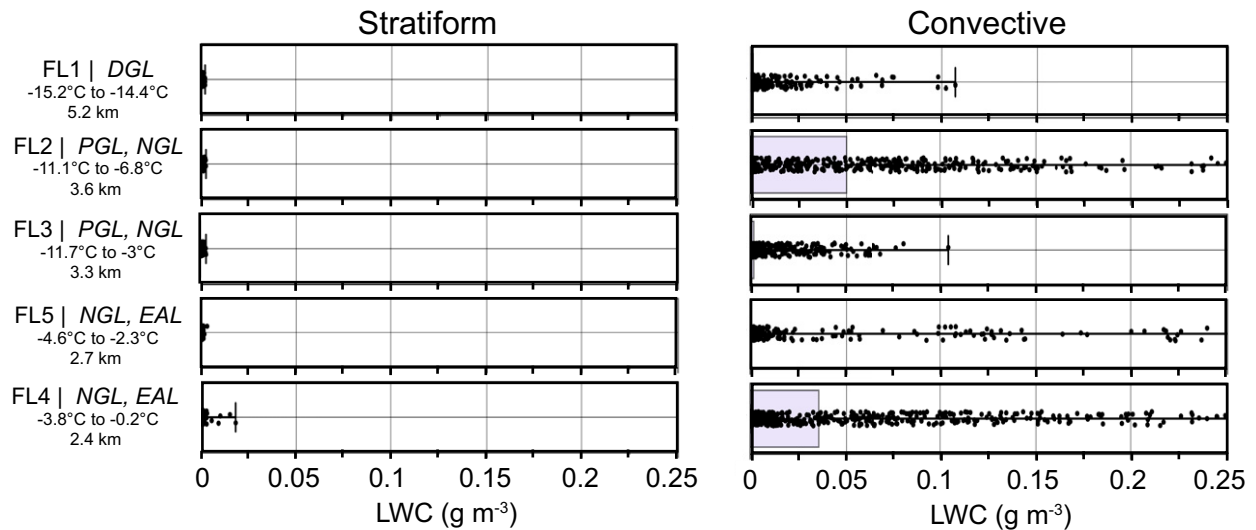


FIG. 15. As in Fig. 11, but for supercooled liquid water content (g m^{-3}). Whiskers represent the maximum data points.

particles), capped columns (2.8% of particles), and graupel (3.7% of particles) (Figs. 18, 19, Table 5). Side planes and other polycrystalline particles likely descended into the DGL from the PCGL aloft, while dendrites formed in situ. PHIPS imagery also contained side plane crystals that had started to grow dendritic structures. Of the PHIPS

particles analyzed, 68.7% were rimed in the CR along FL1. The IWC of the particles in the DGL on FL1 ranged from 0.1 to 2.4 g m^{-3} , with $\text{IWC}_{\text{median}} = 0.6 \text{ g m}^{-3}$ (Fig. 20, Table 6).

FL2 sampled the lower PGL and upper NGL (-8.6° to -5.4°C) at an altitude of 3.6 km. On this leg, N_r ranged from 0.1 to 59.4 L^{-1} with $N_{\text{median}} = 7.5 \text{ L}^{-1}$ (from 0.1 to 57.5 L^{-1} with

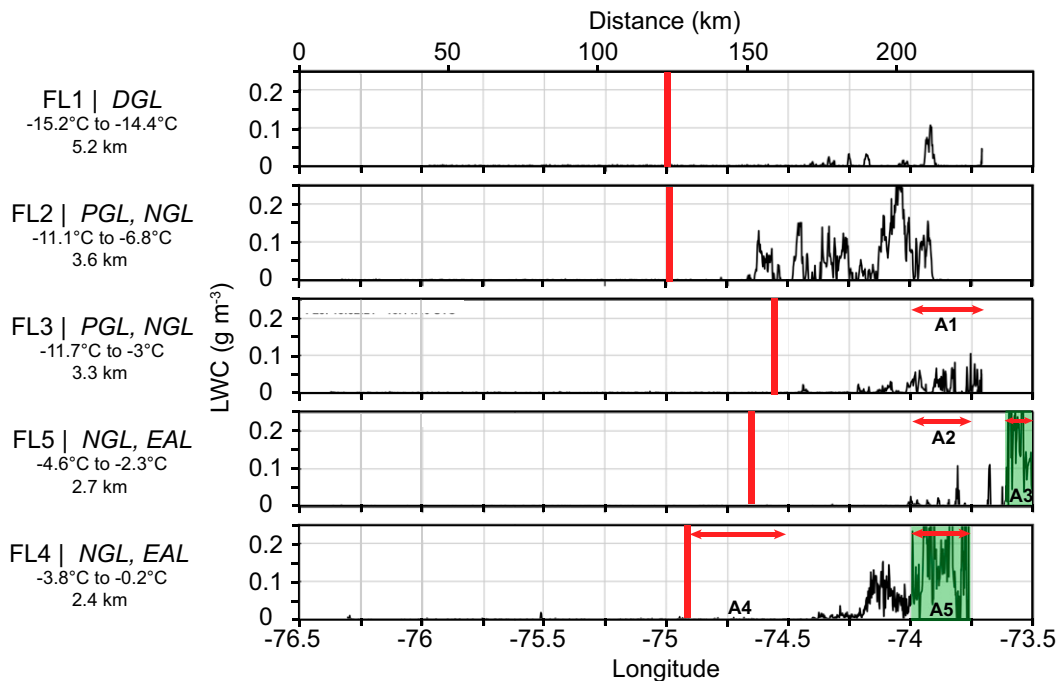


FIG. 16. Supercooled liquid water content (g m^{-3}) across the P-3 flight track measured by the CDP for all five flight legs. The red solid line along each flight leg separates the stratiform region and convective region and was determined using microphysics data. Red arrows are subsets of microphysical data that will be shown in Fig. 21. Green shaded areas are regions where raindrops were observed.

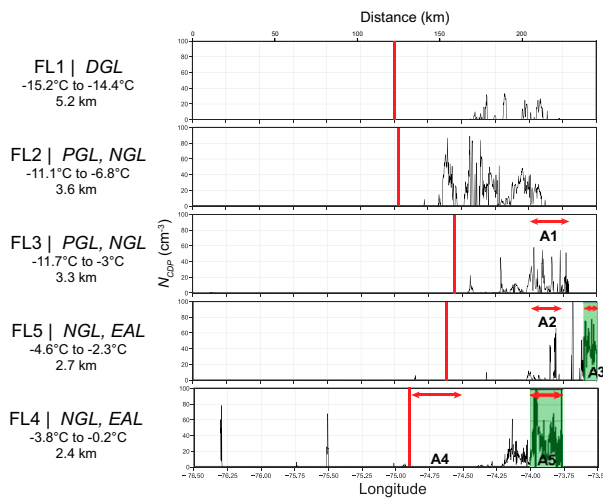


FIG. 17. As in Fig. 16, except CDP N_{CDP} (cm^{-3}) is shown.

$N_{\text{median}} = 7.5 \text{ L}^{-1}$ for dead time ≤ 0.2 s (Figs. 11–13, Table 3). The mean PSD across the CR on this leg had $N_{2DS} = 7.3 \text{ L}^{-1}$ (7.1 L^{-1} for dead time ≤ 0.2 s) and $N_{HVPS} = 0.8 \text{ L}^{-1}$ (Fig. 14). Droplet concentrations ranged from 10 to 80 cm^{-3} across the

CR with SLW ranging from 0.01 to 0.25 g m^{-3} . Again, a mix of particle habits were observed including side planes (27.5% of particles), polycrystalline and platelike particles (28.9% of particles), columns (14.3% of columns), capped columns (6.5% of particles), and plate–column mixes (6.2% of particles), dendrites (5.7% of particles), and needles (1.3% of particles) (Figs. 18, 19, Table 5), implying that particle formation occurred within the PGL and upper NGL. Of the PHIPS particles analyzed, 67.5% were rimed. IWC ranged from 0.1 to 2.0 g m^{-3} , with $IWC_{\text{median}} = 0.3 \text{ g m}^{-3}$ (Fig. 20, Table 6).

FL3 sampled the NGL and upper EAL (-7.7° to -2.2°C) at an altitude of 3.3 km. N_i ranged from 2.8 to 174.1 L^{-1} with $N_{\text{median}} = 11.9 \text{ L}^{-1}$ (from 2.8 to 172.3 L^{-1} with $N_{\text{median}} = 10.9 \text{ L}^{-1}$ for dead time ≤ 0.2 s) (Figs. 11–13, Table 3). The mean PSD was $N_{2DS} = 19.8 \text{ L}^{-1}$ (16.7 L^{-1} for dead time ≤ 0.2 s) and $N_{HVPS} = 2.1 \text{ L}^{-1}$. The maximum value of N_{2DS} increased substantially from FL2 to FL3, which sampled more of the NGL along the cross section (Fig. 11, Table 4). N_{2DS} had several peaks in region A1 of FL3 with particle concentrations $> 100 \text{ L}^{-1}$ (Figs. 12, 21). The CDP probe detected SLW $> 0.20 \text{ g m}^{-3}$, mainly east of -74.75° longitude (Figs. 15–17) with droplet concentrations ranging from 10 to 60 cm^{-3} on FL3 (Fig. 17). PHIPS stereo-

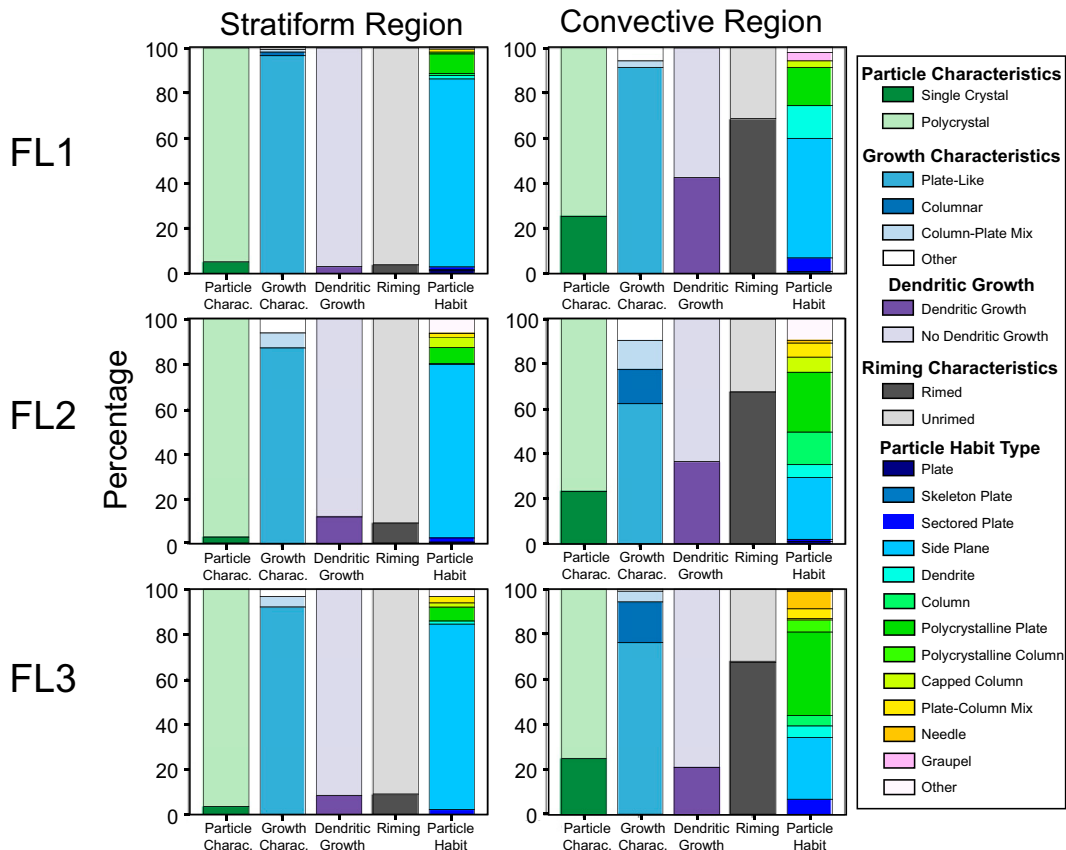
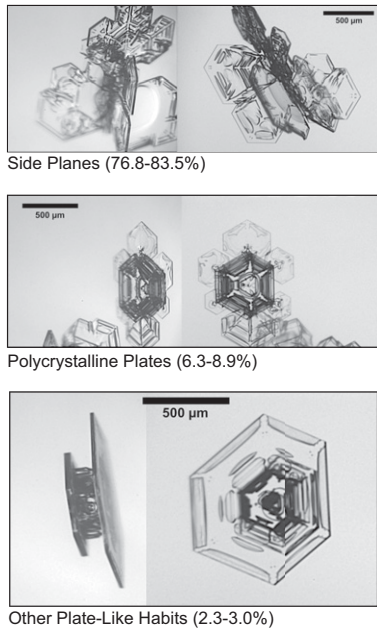


FIG. 18. PHIPS stereo-image statistics in the SR and CR for FL 1–3 (see Table 5), based on the number of particles sampled, particle growth characteristics, particle riming, particle dendritic growth, and particle habits.

Common Habits in the Stratiform Region



Common Habits in the Convective Region

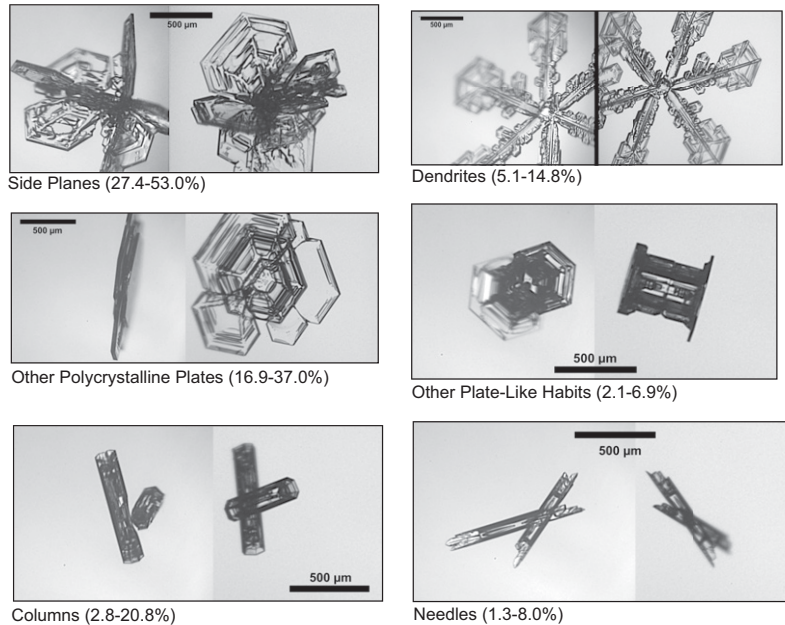


FIG. 19. Representative particle images from the PHIPS probe in (left) the stratiform region of each particle growth layer and (right) the convective region.

imagery analysis revealed that habits were primarily side planes (27.4% of particles), other polycrystalline plates (37.0% of particles) and single plates (6.8% of particles), needles (8.0% of particles), columns (4.6% of particles), capped columns (1.7% of particles), and other plate-column mixes (9.5% of particles), and dendrites (5.1% of particles) (Figs. 18, 19, Table 5). Secondary ice production, either by the Hallett–Mossop (Hallett and Mossop 1974), droplet shattering (e.g., Mason and Maybank 1960; Brownscombe and Thorndike 1968), or the crystal–crystal collision (e.g., Phillips et al. 2017a,b) process likely contributed to enhanced values of N_r . This was qualitatively supported by the presence of needles, columns, and rimed particles. Of the PHIPS particles analyzed, 67.8% were rimed. IWC ranged from 0.0 to 2.0 g m^{-3} , with $\text{IWC}_{\text{median}} = 0.8 \text{ g m}^{-3}$ (Fig. 20, Table 6).

FL4 and FL5 sampled the NGL and EAL at altitudes of 2.4 km (-3.7° to -0.2°C) and 2.7 km (-5.0° to -0.7°C). In the NGL and EAL, N_r ranged from 3.0 to 140.5 L^{-1} with $N_{\text{median}} = 16.7 \text{ L}^{-1}$ on FL4 and from 0.1 to 121.7 L^{-1} with $N_{\text{median}} = 11.5 \text{ L}^{-1}$ on FL5 (Figs. 11–13, Table 3). The PSDs had $N_{2\text{DS}} = 20.9 \text{ L}^{-1}$ and $N_{\text{HVPS}} = 1.7 \text{ L}^{-1}$ for FL4 and $N_{2\text{DS}} = 15.3 \text{ L}^{-1}$ and $N_{\text{HVPS}} = 1.4 \text{ L}^{-1}$ for FL5 (Fig. 14, Table 4). Only localized values of SLW (0.01–0.15 g m^{-3}) were observed at lower altitudes in the CR (Figs. 15–17). Particle habits sampled during FL4 and FL5 in the CR were consistent with previous altitudes with an increase in particle aggregation (Fig. 14). Regions A2 and A4 had enhanced particle concentrations consistent with the process of secondary ice formation with N_r ranging from 40 to 120 L^{-1} (Figs. 12, 21). IWC ranged from

0.0 to 2.2 g m^{-3} , with $\text{IWC}_{\text{median}} = 0.7 \text{ g m}^{-3}$ on FL4 and from 0.0 to 1.8 g m^{-3} , with $\text{IWC}_{\text{median}} = 0.8 \text{ g m}^{-3}$ on FL5 (Fig. 20, Table 6). Region A3 on FL5 and A5 on FL4 (Figs. 12, 13, 16, and 17, Table 2) were periods when droplets were observed within the PHIPS stereo imagery. During these periods small drizzle drops were apparently being lofted through the 0°C isotherm.

The measurements in the CR show that water saturation was achieved in convective turrets allowing for the formation and growth of new particles at all altitudes (Figs. 15–17). Supercooled liquid water was present at cloud top based on an analysis of lidar returns at cloud top. At the same time, side planes and polycrystalline particles formed in the upper part of the cloud above the highest flight level and fell through the DGL, PGL, NGL, and EAL. The presence of supercooled liquid water allowed a large percentage of these particles to become rimed. These observations are also consistent with the action of secondary ice production at temperatures between -8° and -3°C leading to higher particle concentrations and the growth of needles and columns which subsequently aggregated.

6. Nature of the precipitation band

Figure 3 shows a band of higher reflectivity at 2.5-km altitude within the comma head. The band appeared on the cross section near -75° longitude at 1500 UTC (Fig. 9) and was within the 2.5-km region of high correlation coefficient (>0.96 , Fig. 3), indicating ice at that level. The band aligned with the axis of maximum 700-hPa kinematic frontogenesis

TABLE 5. PHIPS stereo-image statistics corresponding to columns in Fig. 18 for FL 1–3. Statistics are based on the number of particles sampled, particle growth characteristics, particle riming, particle dendritic growth, and particle habits.

	SR FL1	CR FL1	SR FL2	CR FL2	SR FL3	CR FL3
Particles sampled and characteristics						
No. of particles sampled	1293	1576	1934	1022	2286	1023
No. of particles analyzed	665	575	655	385	783	351
Single crystal proportion	5.1%	25.2%	3.2%	23.4%	3.7%	24.8%
Polycrystal proportion	94.9%	75.8%	96.8%	76.6%	96.3%	75.2%
Growth characteristics						
Platelike	96.5%	91.5%	87.2%	62.1%	92.1%	76.3%
Columnar	1.7%	0.0%	0.0%	15.6%	0.0%	17.9%
Column–plate mix	1.2%	3.0%	6.3%	12.7%	4.6%	4.8%
Other	0.0%	5.5%	6.5%	9.6%	3.3%	1.0
Dendritic growth						
Dendritic growth	3.0%	42.4%	12.2%	36.6%	8.6%	21.1%
No dendritic growth	97.0%	57.6%	87.8%	63.4%	91.4%	78.9%
Riming characteristics						
Rimed	3.9%	68.7%	9.3%	67.5%	9.1%	67.8%
Unrimed	96.1%	31.3%	90.7%	32.5%	90.9%	32.2%
Individual habit proportions						
Plate	1.4%	0.4%	0.5%	1.3%	0.1%	0.3%
Skeleton plate	0.2%	0.4%	0.3%	0.0	0.3%	0.0%
Sectored plate	1.4%	6.1%	2.1%	0.8%	1.9%	6.6%
Side plane	83.5%	53.0%	76.8%	27.5%	82.2%	27.4%
Dendrite	1.4%	14.8%	0.3%	5.7%	1.4%	5.1%
Column	0.0%	0.0%	0.0%	14.3%	0.0%	4.6%
Other: Polycrystalline plate	8.9%	16.9%	7.2%	26.8%	6.3%	37.0%
Other: Polycrystalline column	0.8%	0.0%	0.0%	0.0%	0.0%	5.4%
Capped column	1.2%	2.8%	4.4%	6.5%	1.7%	0.6%
Other: Plate–column mix	0.0%	0.2%	1.8%	6.2%	2.9%	4.3%
Needle	0.0%	0.0%	0.0%	1.3%	0.0%	8.0%
Graupel	0.0%	3.7%	0.0%	0.0%	0.0%	0.3%
Other	0.6%	1.9%	6.6%	9.6%	3.3%	0.6%

suggesting that vertical circulations associated with frontogenesis might be important. Examining Fig. 10, the maximum synoptic-scale vertical motion indeed occurred above the region of maximum frontogenesis (Fig. 4c). The band was in the SR near the boundary between the SR and CR, and the Z_e values were the highest anywhere within the SR. The cross section in Fig. 9 shows that even higher Z_e associated with the band was present at altitudes below the region of maximum frontogenesis. A key to understanding the nature of this region appears in Fig. 9, where the highest Z_e values were collocated with negative radial velocities of $\sim -4 \text{ m s}^{-1}$, values consistent with those in the melting layer farther to the east.

These observations together indicate that the band was the result of enhanced growth of ice particles within the SR within the region of increased synoptic-scale vertical motion associated with frontogenesis. Although not observed, it is likely that these particles aggregated as they approached a warm zone of air near the surface and then melted or partially melted, creating large wet snowflakes and the high Z_e near the ground. Unfortunately, the P-3 was unable to fly low

enough to sample this region and confirm this hypothetical chain of events.

7. Summary

This paper examined the microphysical evolution of precipitation in the context of storm frontal structure and kinematics across the comma-head region of a northeastern U.S. snowstorm. Although past studies have shown that many of these storms have convective and stratiform regions, the evolution of precipitation within these regions within northeast snowstorms, to our knowledge, has never been investigated in situ and interpreted in the context of airborne radar observations and frontal structure.

The 7 February 2020 winter storm was a rapidly deepening extratropical cyclone that exhibited different precipitation growth processes within the comma-head region. The storm was observed using two aircraft as part of the NASA Investigation of Microphysics and Precipitation for Atlantic Coast-Threatening Snowstorms (IMPACTS) field campaign. From a synoptic-scale perspective, a convective region developed as

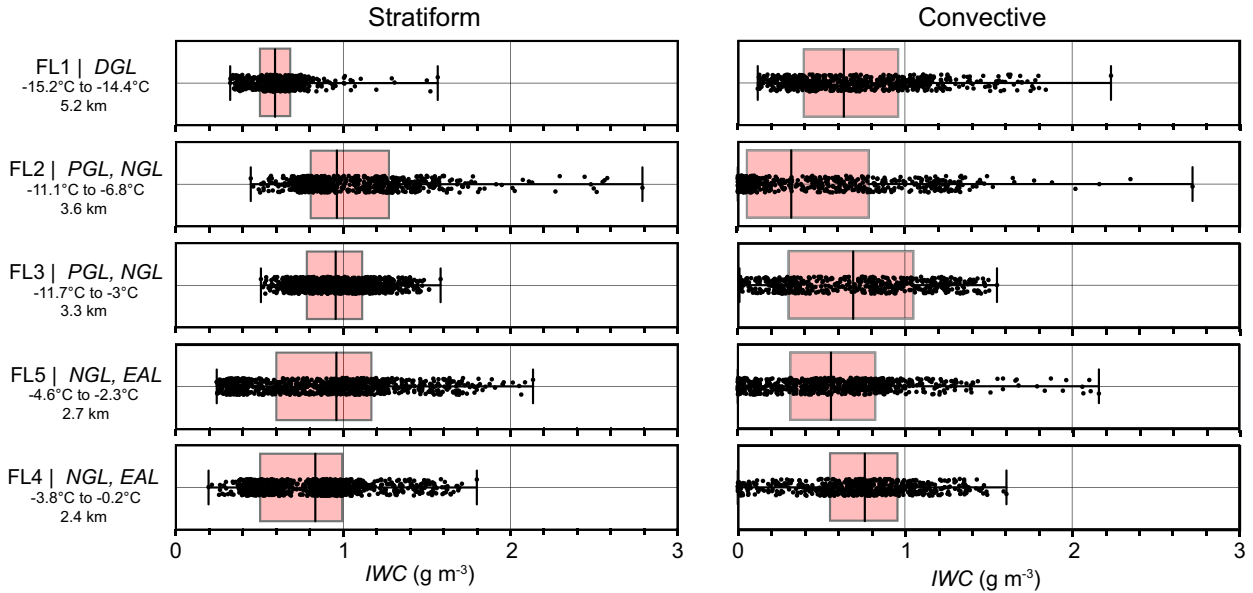


FIG. 20. As in Fig. 11, but for total ice water content (g m^{-3}). Percentiles can be found in Table 5. Whiskers represent the mean ± 1.5 times the interquartile range.

unsaturated air within the cyclone’s dry slot moved over the cloud layer ascending over the cyclone’s warm front. A stratiform region occurred west of the impinging dry-slot airstream. This resulted in two distinct microphysical regions across the comma head. The distinction between these regions was evident in the high-resolution reflectivity and radial velocity characteristics observed in the ER-2 radar profiles. Reflectivity towers with updrafts of $1\text{--}2 \text{ m s}^{-1}$ were observed in the upper cloud layer within the convective region with corresponding plumes of reflectivity descending into the lower cloud; while the stratiform region was characterized by a more uniform reflectivity gradient both horizontally and vertically, and weaker vertical circulations near cloud top.

The microphysical evolution of particles within the CR differed from the SR. Differences between the SR and CR are summarized in an idealized conceptual model in Fig. 22. In the SR, observations support the formation of ice crystals in the polycrystalline growth layer near cloud top. As ice crystals

fell through subsequent particle growth layers, the observations were consistent with particle growth by vapor deposition, quantitatively supported by an overall slight increase in IWC with depth between the aircraft flight levels (Fig. 20). Very few new particle habits were observed in the PHIPS stereo images implying that new particle formation was rare at lower altitudes within the SR. This was quantitatively confirmed by the lack of variation in the statistical distribution of N_i with depth between the aircraft flight levels within the cloud (Figs. 11–13).

In the CR, new particle habits (e.g., dendrites, columns, needles) were observed within each temperature-defined growth layer along with detectable amounts of supercooled liquid water, consistent with ice particle formation in several particle growth layers. Updrafts within the CR penetrated through the polycrystalline growth layer and dendritic growth layer and were a source of SLW throughout the upper cloud layer. SLW was present in developing convective cells and was sampled at different heights on numerous flight legs.

TABLE 6. Measurements of IWC (g m^{-3}) for the minimum (IWC_{\min}), 25th-percentile (IWC_{25}), 50th-percentile (IWC_{50}), 75th-percentile (IWC_{75}), and maximum (IWC_{\max}) values in the stratiform and convective regions corresponding to Fig. 20.

Flight leg	Particle growth layer	Stratiform region					Convective region					
		IWC_{\min}	IWC_{25}	IWC_{50}	IWC_{75}	IWC_{\max}	Particle growth layer	IWC_{\min}	IWC_{25}	IWC_{50}	IWC_{75}	IWC_{\max}
1	DGL	0.5	0.6	0.8	0.9	1.7	DGL	0.1	0.4	0.6	1.1	2.4
2	PGL	0.4	0.8	1.1	1.4	2.9	PGL, NGL	0.0	0.1	0.3	0.8	2.7
3	PGL	0.6	0.9	1.1	1.2	1.7	PGL, NGL	0.1	0.4	0.8	1.2	2.0
5	NGL	0.3	0.5	0.9	1.0	1.8	NGL, EAL	0.0	0.6	0.8	1.0	1.8
4	NGL	0.2	0.6	1.0	1.2	2.1	NGL, EAL	0.0	0.5	0.7	0.9	2.2

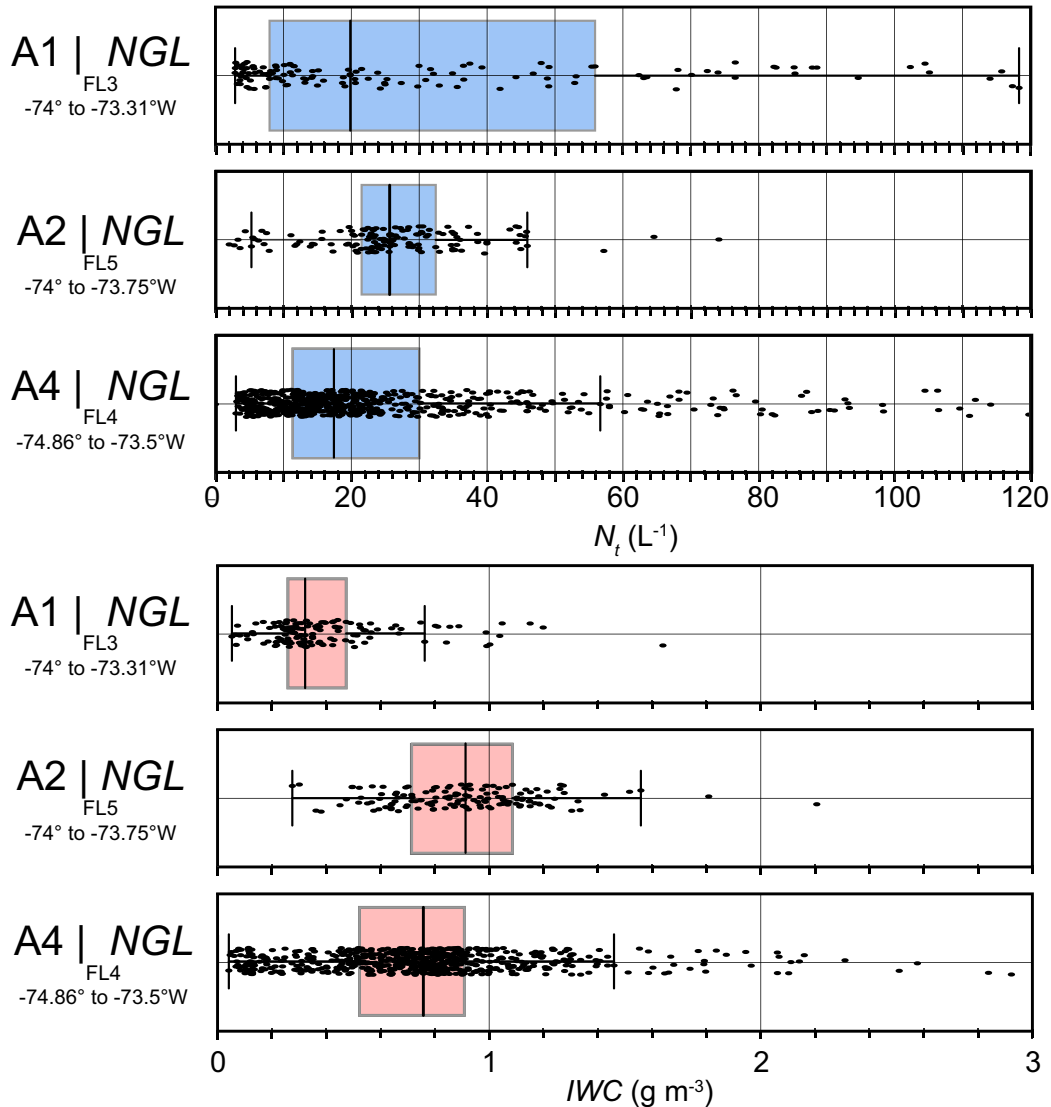


FIG. 21. Total number concentration (L^{-1} ; blue) and total ice water content ($g\ m^{-3}$; red) during periods of enhanced concentrations due to needle growth. Whiskers represent the mean ± 1.5 times the interquartile range. The regions A1, A2, and A4 refer to Figs. 12, 13, 16, and 17.

As the cells evolved and matured, SLW was converted to ice. At higher temperatures (-8° to $-3^{\circ}C$) sampled during the flight, pockets with ice particle concentrations exceeding $100\ L^{-1}$ were present, consistent with secondary ice production at these altitudes. Expected particle habits associated with secondary ice production, specifically heavily rimed particles together with columns and needles and supercooled drizzle drops (e.g., Luke et al. 2021), provided supportive evidence.

Figure 23 shows the total surface precipitation across New York State for the period of 1400–1800 UTC. Total precipitation (rain + snow) was generally larger near the transition zone between the SR and CR during the time period of the flight. WSR-88D reflectivity composites during the flight sampling period showed a weak, banded

feature. The band, evident most prominently on earlier flight legs, was shown to be associated with enhanced vertical motion associated with frontogenesis, followed by particle aggregation and subsequent melting (likely partial melting) of ice particles near the surface. This band coincided with the maximum in total precipitation during the period.

As noted in the introduction, the comma heads of extratropical cyclones over the eastern United States have previously been shown to often exhibit an elevated layer of potential instability and convection on their warm sides, and stable air, often topped by shallow convective cloud-top generating cells on their cold sides. This study provides the first in situ quantitative microphysical analysis of the stratiform and elevated convective regions of the comma head of a

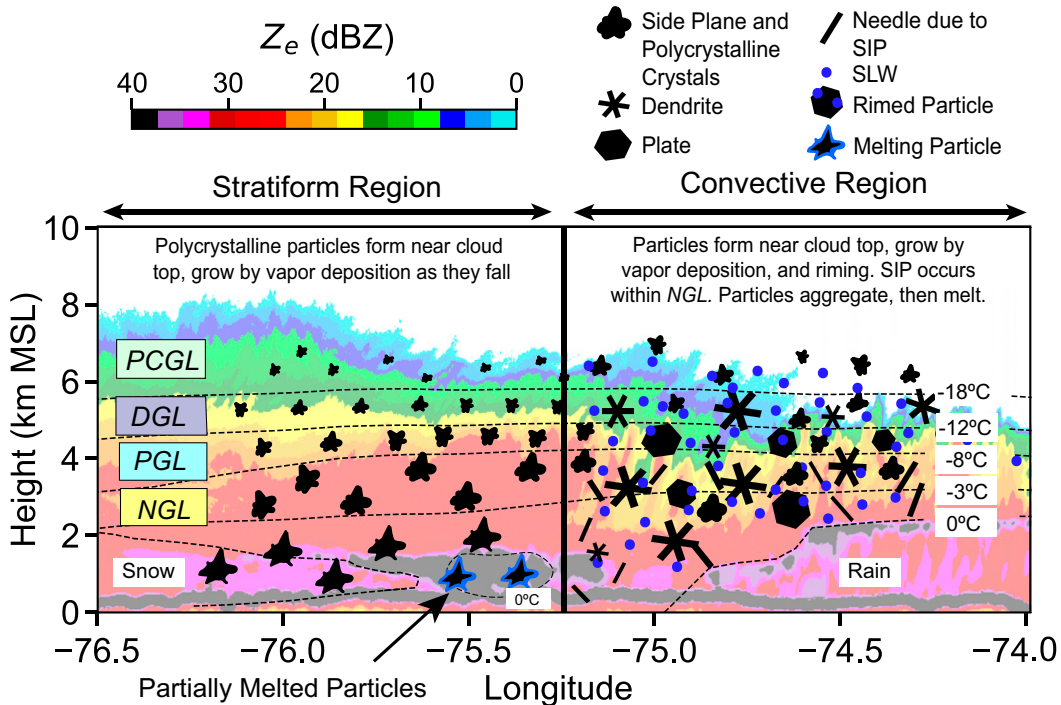


FIG. 22. Conceptual model of precipitation processes in the stratiform region and convective region. Particle habits are represented by black shapes and are denoted above the figure. SLW is represented by blue dots. SLW was present in developing convective cells but converted to ice as the cells matured. The region denoted partially melted particles is the location of the band on the WSR-88D composite.

northeastern U.S. winter cyclone. The IMPACTS project is a 3-yr effort to further document and understand the range of microphysical scenarios that occur in cyclones with a range of intensities and banded organization over the northeastern

United States. Future work using a similar framework will allow exploration of particle growth mechanisms within a variety of synoptic environments.

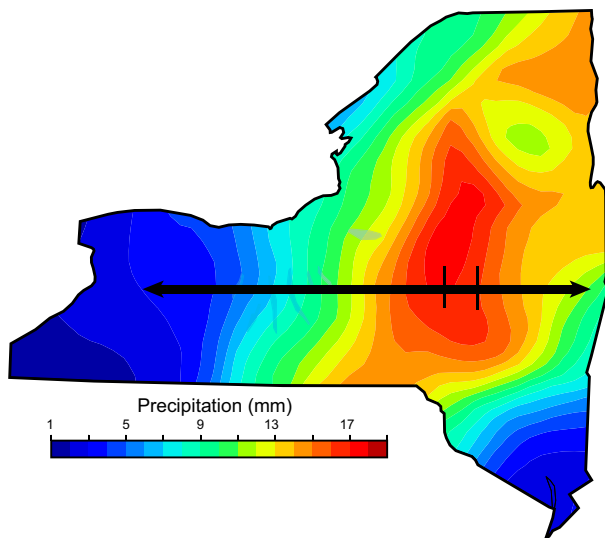


FIG. 23. Total precipitation between 1400 and 1800 UTC 7 Feb 2020 from the New York State Mesonet (Brotzge et al. 2020). The dark horizontal line with the arrows represents the flight track and the black vertical lines are the westernmost and easternmost positions of the SR-CR boundary as determined from the microphysical analysis.

Acknowledgments. Field campaigns of this size depend on the dedication and support of many individuals and institutions. We thank everyone involved in the planning, execution, and support of the IMPACTS field campaign. We also thank the NASA Earth Science Division (ESD) and Earth Venture Sub-orbital Program under the NASA Airborne Science Program for their support of this program. We especially thank the crews from the NASA P-3 Orion and the NASA Earth Resources 2 aircraft. This work was funded by the NASA Earth Venture Suborbital-3 (EVS-3) program under Grants 80NSSC19K0355 (UIUC), 80NSSC19K0338 (UW), 80NSSC19K0399 (OU), and 80NSSC19K0328 (UND). This work has also received funding from the Helmholtz Research Program Atmosphere and Climate and by the German Research Foundation (DFG Grant JA 2818/1-1). The PHIPS deployment during IMPACTS was based on a collaboration agreement between NASA and KIT. We thank three anonymous reviewers for comments and suggestions that helped substantially improve the quality of the paper.

Data availability statement. All IMPACTS quick-look images and mission scientist reports from the 2020 deployment are highlighted in the IMPACTS field catalog at http://catalog.eol.ucar.edu/impacts_2020 and the data can be obtained from

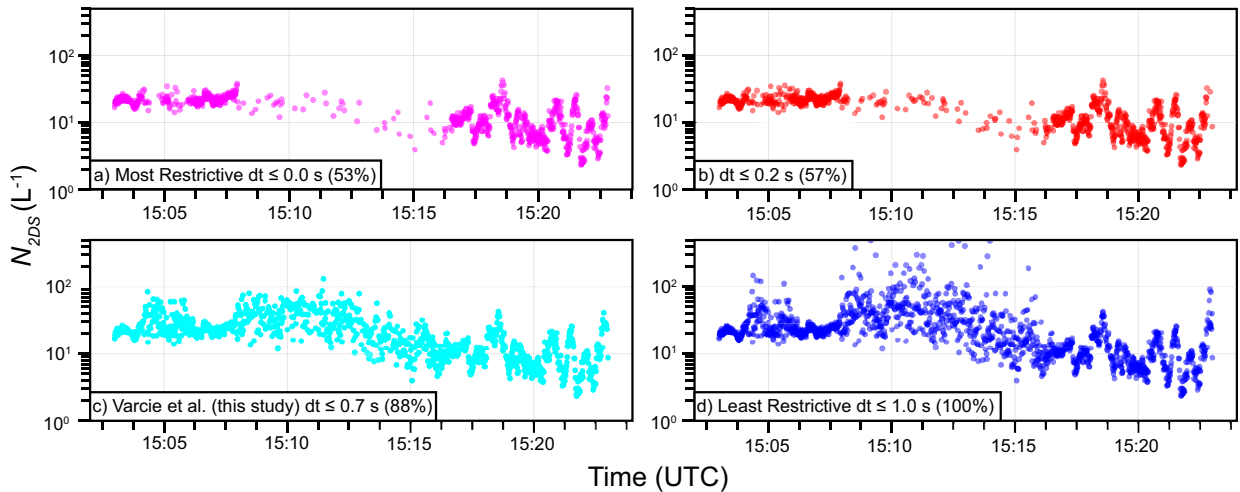


FIG. A1. N_{2DS} (L^{-1}) measured for each 1-Hz sample for different dead-time thresholds for FL1. Each dot represents one measurement. (a) Most restrictive threshold (dead time = 0.0 s), (b) dead time ≤ 0.2 s, (c) dead time ≤ 0.7 s, and (d) the least restrictive threshold (dead time ≤ 1.0 s). The threshold with dead time ≤ 0.7 s was used in this paper.

the Global Hydrology Resource Center Distributed Active Archive Center at https://ghrc.nsstc.nasa.gov/uso/ds_details/collections/impactsC.html and [McMurdie et al. \(2019\)](#).

APPENDIX

Assessment of Dead-Time Thresholds

Figure A1 shows the differences in the amount of data for N_{2DS} available for 1-s periods when different dead-time thresholds are applied on FL1. Note that as the dead-time threshold increases, N_{2DS} has a progressively greater spread (standard deviation of $11 L^{-1}$ for dead time ≤ 0.7 s and a standard deviation of $6 L^{-1}$ for dead time ≤ 0.2 s). It is uncertain how reliable the calculation of N_{2DS} is for time periods with large dead time. In this paper periods with dead time ≤ 0.7 s are included in plots and the calculated concentrations. However, all points with dead time > 0.2 s are flagged because more uncertainty in the calculated concentrations exist. For flight levels where more than 20% of the 1-s time periods have dead times > 0.2 s, separate statistics on N_{2DS} are provided using a more conservative dead-time threshold (≤ 0.2 s). Another approach to reduce the uncertainty caused by dead time is to average over longer time periods and choose a less restrictive dead time. For example, [Dunnavan et al. \(2022\)](#) used this approach when comparing radar data from the WSR-88D network to microphysical observations made during the 7 February 2020 case. [Finlon et al. \(2022\)](#) also used this approach in their comparison of enhanced regions of dual-frequency ratios to microphysical properties during the 7 February 2020 case. In these cases, averaging was appropriate because they were comparing to the large sample volumes associated with ground-based and airborne radars.

REFERENCES

- Abdelmonem, A., E. Järvinen, D. Duft, E. Hirst, S. Vogt, T. Leisner, and M. Schnaiter, 2016: PHIPS–HALO: The airborne Particle Habit Imaging and Polar Scattering probe. Part 1: Design and operation. *Atmos. Meas. Tech.*, **9**, 3131–3144, <https://doi.org/10.5194/amt-9-3131-2016>.
- Bailey, M. P., and J. Hallett, 2009: A comprehensive habit diagram for atmospheric ice crystals: Confirmation from the laboratory, AIRS II, and other field studies. *J. Atmos. Sci.*, **66**, 2888–2899, <https://doi.org/10.1175/2009JAS2883.1>.
- Baker, B., and R. P. Lawson, 2006: Improvement in determination of ice water content from two-dimensional particle imagery. Part I: Image-to-mass relationships. *J. Appl. Meteor. Climatol.*, **45**, 1282–1290, <https://doi.org/10.1175/JAM2398.1>.
- Baumgardner, D., and A. Rodi, 1989: Laboratory and wind tunnel evaluations of the Rosemount Icing Detector. *J. Atmos. Oceanic Technol.*, **6**, 971–979, [https://doi.org/10.1175/1520-0426\(1989\)006<0971:LAWTEO>2.0.CO;2](https://doi.org/10.1175/1520-0426(1989)006<0971:LAWTEO>2.0.CO;2).
- Benjamin, S. G., and Coauthors, 2016: A North American hourly assimilation and model forecast cycle: The Rapid Refresh. *Mon. Wea. Rev.*, **144**, 1669–1694, <https://doi.org/10.1175/MWR-D-15-0242.1>.
- Broetzge, J. A., and Coauthors, 2020: A technical overview of the New York State Mesonet standard network. *J. Atmos. Oceanic Technol.*, **37**, 1827–1845, <https://doi.org/10.1175/JTECH-D-19-0220.1>.
- Brownscombe, J. L., and N. S. C. Thorndike, 1968: Freezing and shattering of water droplets in freefall. *Nature*, **220**, 687–689, <https://doi.org/10.1038/220687a0>.
- Cober, S. G., G. A. Isaac, and J. W. Strapp, 2001: Characterizations of aircraft icing environments that include supercooled large drops. *J. Appl. Meteor.*, **40**, 1984–2002, [https://doi.org/10.1175/1520-0450\(2001\)040<1984:COAIET>2.0.CO;2](https://doi.org/10.1175/1520-0450(2001)040<1984:COAIET>2.0.CO;2).
- Colle, B. A., D. Stark, and S. E. Yuter, 2014: Surface microphysical observations within East Coast winter storms on Long Island, New York. *Mon. Wea. Rev.*, **142**, 3126–3146, <https://doi.org/10.1175/MWR-D-14-00035.1>.
- Dunnavan, E. L., and Coauthors, 2022: Radar retrieval evaluation and investigation of dendritic growth layer polarimetric

- signatures in a winter storm. *J. Appl. Meteor. Climatol.*, **61**, 1685–1711, <https://doi.org/10.1175/JAMC-D-21-0220.1>.
- Evans, A. G., J. D. Locatelli, M. T. Stoelinga, and P. V. Hobbs, 2005: The IMPROVE-1 storm of 1–2 February 2001. Part II: Cloud structures and the growth of precipitation. *J. Atmos. Sci.*, **62**, 3456–3473, <https://doi.org/10.1175/JAS3547.1>.
- Field, P. R., A. J. Heymsfield, and A. Bansemmer, 2006: A test of ice self-collection kernels using aircraft data. *J. Atmos. Sci.*, **63**, 651–666, <https://doi.org/10.1175/JAS3653.1>.
- Finlon, J. A., G. M. McFarquhar, S. W. Nesbitt, R. M. Rauber, H. Morrison, W. Wu, and P. Zhang, 2019: A novel approach to characterize the variability in mass–dimension relationships: Results from MC3E. *Atmos. Chem. Phys.*, **19**, 3621–3643, <https://doi.org/10.5194/acp-19-3621-2019>.
- , L. A. McMurdie, and R. J. Chase, 2022: Investigation of microphysical properties within regions of enhanced dual-frequency ratio during the IMPACTS field campaign. *J. Atmos. Sci.*, **79**, 2773–2795, <https://doi.org/10.1175/JAS-D-21-0311.1>.
- Ganetis, S. A., B. A. Colle, S. E. Yuter, and N. P. Hoban, 2018: Environmental conditions associated with observed snow-band structures within northeast U.S. winter storms. *Mon. Wea. Rev.*, **146**, 3675–3690, <https://doi.org/10.1175/MWR-D-18-0054.1>.
- Grasmick, C., and B. Geerts, 2020: Detailed dual-Doppler structure of Kelvin–Helmholtz waves from an airborne profiling radar over complex terrain. Part I: Dynamic structure. *J. Atmos. Sci.*, **77**, 1761–1782, <https://doi.org/10.1175/JAS-D-19-0108.1>.
- Grim, J. A., R. M. Rauber, M. K. Ramamurthy, B. F. Jewett, and M. Han, 2007: High-resolution observations of the trowal–warm-frontal region of two continental winter cyclones. *Mon. Wea. Rev.*, **135**, 1629–1646, <https://doi.org/10.1175/MWR3378.1>.
- Guan, H., S. G. Cober, and G. A. Isaac, 2001: Verification of supercooled cloud forecasts within situ aircraft measurements. *Wea. Forecasting*, **16**, 145–155, [https://doi.org/10.1175/1520-0434\(2001\)016<0145:VOSCWF>2.0.CO;2](https://doi.org/10.1175/1520-0434(2001)016<0145:VOSCWF>2.0.CO;2).
- Gunn, K. L. S., and J. S. Marshall, 1958: The distribution with size of aggregate snowflakes. *J. Atmos. Sci.*, **15**, 452–461, [https://doi.org/10.1175/1520-0469\(1958\)015<0452:TDWSOA>2.0.CO;2](https://doi.org/10.1175/1520-0469(1958)015<0452:TDWSOA>2.0.CO;2).
- Hallett, J., and S. C. Mossop, 1974: Production of secondary ice particles during the riming process. *Nature*, **249**, 26–28, <https://doi.org/10.1038/249026a0>.
- Han, M., R. M. Rauber, M. K. Ramamurthy, B. F. Jewett, and J. A. Grim, 2007: Mesoscale dynamics of the trowal and warm-frontal regions of two continental winter cyclones. *Mon. Wea. Rev.*, **135**, 1647–1670, <https://doi.org/10.1175/MWR3377.1>.
- Herzogh, P. H., and P. V. Hobbs, 1980: The mesoscale and microscale structure and organization of clouds and precipitation in midlatitude cyclones. II: Warm-frontal clouds. *J. Atmos. Sci.*, **37**, 597–611, [https://doi.org/10.1175/1520-0469\(1980\)037<0597:TMAMSA>2.0.CO;2](https://doi.org/10.1175/1520-0469(1980)037<0597:TMAMSA>2.0.CO;2).
- , and —, 1981: The mesoscale and microscale structure and organization of clouds and precipitation in midlatitude cyclones. IV: Vertical air motions and microphysical structures of prefrontal surge clouds and cold-frontal clouds. *J. Atmos. Sci.*, **38**, 1771–1784, [https://doi.org/10.1175/1520-0469\(1981\)038<1771:TMAMSA>2.0.CO;2](https://doi.org/10.1175/1520-0469(1981)038<1771:TMAMSA>2.0.CO;2).
- Heymsfield, A. J., and J. L. Parrish, 1978: A computational technique for increasing the effective sampling volume of the PMS two-dimensional particle size spectrometer. *J. Appl. Meteor.*, **17**, 1566–1572, [https://doi.org/10.1175/1520-0450\(1978\)017<1566:ACTFIT>2.0.CO;2](https://doi.org/10.1175/1520-0450(1978)017<1566:ACTFIT>2.0.CO;2).
- Hobbs, P. V., and A. L. Rangno, 1998: Microstructures of low and middle-level clouds over the Beaufort Sea. *Quart. J. Roy. Meteor. Soc.*, **124**, 2035–2071, doi:10.1002/qj.49712455012.
- , T. J. Matejka, P. H. Herzogh, J. D. Locatelli, and R. A. Houze Jr., 1980: The mesoscale and microscale structure and organization of clouds and precipitation in midlatitude cyclones. I: A case study of a cold front. *J. Atmos. Sci.*, **37**, 568–596, [https://doi.org/10.1175/1520-0469\(1980\)037<0568:TMAMSA>2.0.CO;2](https://doi.org/10.1175/1520-0469(1980)037<0568:TMAMSA>2.0.CO;2).
- Houze, R. A., Jr., J. D. Locatelli, and P. V. Hobbs, 1976a: Dynamics and cloud microphysics of the rainbands in an occluded frontal system. *J. Atmos. Sci.*, **33**, 1921–1936, [https://doi.org/10.1175/1520-0469\(1976\)033<1921:DACMOT>2.0.CO;2](https://doi.org/10.1175/1520-0469(1976)033<1921:DACMOT>2.0.CO;2).
- , P. V. Hobbs, K. R. Biswas, and W. M. Davis, 1976b: Mesoscale rainbands in extratropical cyclones. *Mon. Wea. Rev.*, **104**, 868–878, [https://doi.org/10.1175/1520-0493\(1976\)104<0868:MRIEC>2.0.CO;2](https://doi.org/10.1175/1520-0493(1976)104<0868:MRIEC>2.0.CO;2).
- , —, P. H. Herzogh, and D. B. Parsons, 1979: Size distributions of precipitation particles in frontal clouds. *J. Atmos. Sci.*, **36**, 156–162, [https://doi.org/10.1175/1520-0469\(1979\)036<0156:SDOPPI>2.0.CO;2](https://doi.org/10.1175/1520-0469(1979)036<0156:SDOPPI>2.0.CO;2).
- , S. A. Rutledge, T. J. Matejka, and P. V. Hobbs, 1981: The mesoscale and microscale structure and organization of clouds and precipitation in midlatitude cyclones. III: Air motions and precipitation growth in a warm-frontal rainband. *J. Atmos. Sci.*, **38**, 639–649, [https://doi.org/10.1175/1520-0469\(1981\)038<0639:TMAMSA>2.0.CO;2](https://doi.org/10.1175/1520-0469(1981)038<0639:TMAMSA>2.0.CO;2).
- Hu, Y., and Coauthors, 2021: Dependence of ice microphysical properties on environmental parameters: Results from HAIC-HIWC Cayenne field campaign. *J. Atmos. Sci.*, **78**, 2957–2981, <https://doi.org/10.1175/JAS-D-21-0015.1>.
- Jackson, R. C., and G. M. McFarquhar, 2014: An assessment of the impact of antishattering tips and artifact removal techniques on cloud ice size distributions measured by the 2D cloud probe. *J. Atmos. Oceanic Technol.*, **31**, 2131–2144, <https://doi.org/10.1175/JTECH-D-14-00018.1>.
- Korolev, A., and G. A. Isaac, 2006: Relative humidity in liquid, mixed-phase, and ice clouds. *J. Atmos. Sci.*, **63**, 2865–2880, <https://doi.org/10.1175/JAS3784.1>.
- , E. F. Emery, J. W. Strapp, S. G. Cober, G. A. Isaac, M. Wasey, and D. Marcotte, 2011: Small ice particle in tropospheric clouds: Fact or artifact? Airborne Icing Instrumentation Evaluation experiment. *Bull. Amer. Meteor. Soc.*, **92**, 967–973, <https://doi.org/10.1175/2010BAMS3141.1>.
- Kumjian, M. R., and K. A. Lombardo, 2017: Insights into the evolving microphysical and kinematic structure of northeastern U.S. winter storms from dual-polarization Doppler radar. *Mon. Wea. Rev.*, **145**, 1033–1061, <https://doi.org/10.1175/MWR-D-15-0451.1>.
- Lance, S., 2012: Coincidence errors in a Cloud Droplet Probe (CDP) and a Cloud and Aerosol Spectrometer (CAS), and the improved performance of a modified CDP. *J. Atmos. Oceanic Technol.*, **29**, 1532–1541, <https://doi.org/10.1175/JTECH-D-11-00208.1>.
- , C. A. Brock, D. Rogers, and J. A. Gordon, 2010: Water droplet calibration of the Cloud Droplet Probe (CDP) and in-flight performance in liquid, ice and mixed-phase clouds during ARCPAC. *Atmos. Meas. Tech.*, **3**, 1683–1706, <https://doi.org/10.5194/amt-3-1683-2010>.
- Lawson, R. P., R. E. Stewart, J. W. Strapp, and G. A. Isaac, 1993: Aircraft observations of the origin and growth of very large snowflakes. *Geophys. Res. Lett.*, **20**, 53–56, <https://doi.org/10.1029/92GL02917>.

- , —, and L. J. Angus, 1998: Observations and numerical simulations of the origin and development of very large snowflakes. *J. Atmos. Sci.*, **55**, 3209–3229, [https://doi.org/10.1175/1520-0469\(1998\)055<3209:OANSOT>2.0.CO;2](https://doi.org/10.1175/1520-0469(1998)055<3209:OANSOT>2.0.CO;2).
- , D. O'Connor, P. Zmarzly, K. Weaver, B. Baker, Q. Mo, and H. Jonsson, 2006: The 2D-S (stereo) probe: Design and preliminary tests of a new airborne, high-speed, high-resolution particle imaging probe. *J. Atmos. Oceanic Technol.*, **23**, 1462–1477, <https://doi.org/10.1175/JTECH1927.1>.
- Li, L., G. Heymsfield, J. Carswell, D. Schaubert, J. Creticos, and M. Vega, 2008: High-Altitude Imaging Wind and Rain Airborne Radar (HIWRAP). 2008 *IEEE Int. Geoscience and Remote Sensing Symp.*, Boston, MA, IEEE, 354–357, <https://doi.org/10.1109/IGARSS.2008.4779356>.
- Luke, E. P., F. Yang, P. Kollilas, A. M. Vogelmann, and M. Maahn, 2021: New insights into ice multiplication using remote-sensing observations of slightly supercooled mixed-phase clouds in the Arctic. *Proc. Natl. Acad. Sci. USA*, **118**, e2021387118, <https://doi.org/10.1073/pnas.2021387118>.
- Marshall, J. S., 1953: Precipitation trajectories and patterns. *J. Atmos. Sci.*, **10**, 25–29, [https://doi.org/10.1175/1520-0469\(1953\)010<0025:PTAP>2.0.CO;2](https://doi.org/10.1175/1520-0469(1953)010<0025:PTAP>2.0.CO;2).
- Martin, J. E., 1998: The structure and evolution of a continental winter cyclone. Part I: Frontal structure and the occlusion process. *Mon. Wea. Rev.*, **126**, 303–328, [https://doi.org/10.1175/1520-0493\(1998\)126<0303:TSAEOA>2.0.CO;2](https://doi.org/10.1175/1520-0493(1998)126<0303:TSAEOA>2.0.CO;2).
- Mason, B. J., and J. Maybank, 1960: The fragmentation and electrification of freezing water drops. *Quart. J. Roy. Meteor. Soc.*, **86**, 176–185, <https://doi.org/10.1002/qj.49708636806>.
- Matejka, T. J., R. A. Houze Jr., and P. V. Hobbs, 1980: Microphysics and dynamics of clouds associated with mesoscale rainbands in extratropical cyclones. *Quart. J. Roy. Meteor. Soc.*, **106**, 29–56, <https://doi.org/10.1002/qj.49710644704>.
- McFarquhar, G., and Coauthors, 2017: Processing of ice cloud in situ data collected by bulk water, scattering, and imaging probes: Fundamentals, uncertainties, and efforts toward consistency. *Ice Formation and Evolution in Clouds and Precipitation: Measurement and Modeling Challenges, Meteor. Monogr.*, No. 58, Amer. Meteor. Soc., doi:10.1175/AMSMONOGRAPHS-D-16-0007.1.
- , J. A. Finlon, D. M. Stechman, W. Wu, R. C. Jackson, and M. Freer, 2018: University of Illinois/Oklahoma Optical Array Probe (OAP) Processing Software. Zenodo, <https://doi.org/10.5281/zenodo.1285969>.
- McMurdie, L. A., G. Heymesfield, J. E. Yorks, and S. A. Braun, 2019: Investigation of Microphysics and Precipitation for Atlantic Coast-Threatening Snowstorms (IMPACTS) collection. NASA EOSDIS Global Hydrology Resource Center Distributed Active Archive Center, accessed 4 November 2021, <https://doi.org/10.5067/IMPACTS/DATA101>.
- , and Coauthors, 2022: Chasing snowstorms: The Investigation of Microphysics and Precipitation for Atlantic Coast-Threatening Snowstorms (IMPACTS) campaign. *Bull. Amer. Meteor. Soc.*, **103**, E1243–E1269, <https://doi.org/10.1175/BAMS-D-20-0246.1>.
- Murphy, A. M., R. M. Rauber, G. M. McFarquhar, J. A. Finlon, D. M. Plummer, A. A. Rosenow, and B. F. Jewett, 2017: A microphysical analysis of elevated convection in the comma-head region of continental winter cyclones. *J. Atmos. Sci.*, **74**, 69–91, <https://doi.org/10.1175/JAS-D-16-0204.1>.
- Nicosia, D. J., and R. H. Grumm, 1999: Mesoscale band formation in three major northeastern United States snowstorms. *Wea. Forecasting*, **14**, 346–368, [https://doi.org/10.1175/1520-0434\(1999\)014<0346:MBFITM>2.0.CO;2](https://doi.org/10.1175/1520-0434(1999)014<0346:MBFITM>2.0.CO;2).
- NOHRSC, 2022: National gridded snowfall analysis. National Weather Service Office of Water Prediction, accessed 4 November 2021, <https://www.nohrsc.noaa.gov/snowfall/>.
- Novak, D. R., B. A. Colle, and S. E. Yuter, 2008: High-resolution observations and model simulations of the life cycle of an intense mesoscale snowband over the northeastern United States. *Mon. Wea. Rev.*, **136**, 1433–1456, <https://doi.org/10.1175/2007MWR2233.1>.
- , —, and R. McTaggart-Cowan, 2009: The role of moist processes in the formation and evolution of mesoscale snowbands within the comma head of northeast U.S. cyclones. *Mon. Wea. Rev.*, **137**, 2662–2686, <https://doi.org/10.1175/2009MWR2874.1>.
- Passarelli, R. E., Jr., 1978a: An approximate analytical model of the vapor deposition and aggregation growth of snowflakes. *J. Atmos. Sci.*, **35**, 118–124, [https://doi.org/10.1175/1520-0469\(1978\)035<0118:AAAMOT>2.0.CO;2](https://doi.org/10.1175/1520-0469(1978)035<0118:AAAMOT>2.0.CO;2).
- , 1978b: Theoretical and observational study of snow-size spectra and snowflake aggregation efficiencies. *J. Atmos. Sci.*, **35**, 882–889, [https://doi.org/10.1175/1520-0469\(1978\)035<0882:TAOSOS>2.0.CO;2](https://doi.org/10.1175/1520-0469(1978)035<0882:TAOSOS>2.0.CO;2).
- Phillips, V. T. J., J.-I. Yano, and A. Khain, 2017a: Ice multiplication by breakup in ice–ice collisions. Part I: Theoretical formulation. *J. Atmos. Sci.*, **74**, 1705–1719, <https://doi.org/10.1175/JAS-D-16-0224.1>.
- , and Coauthors, 2017b: Ice multiplication by breakup in ice–ice collisions. Part II: Numerical simulations. *J. Atmos. Sci.*, **74**, 2789–2811, <https://doi.org/10.1175/JAS-D-16-0223.1>.
- Plummer, D. M., G. M. McFarquhar, R. M. Rauber, B. F. Jewett, and D. C. Leon, 2014: Structure and statistical analysis of the microphysical properties of generating cells in the comma head region of continental winter cyclones. *J. Atmos. Sci.*, **71**, 4181–4203, <https://doi.org/10.1175/JAS-D-14-0100.1>.
- , —, —, —, and —, 2015: Microphysical properties of convectively generated fall streaks within the stratiform comma head region of continental winter cyclones. *J. Atmos. Sci.*, **72**, 2465–2483, <https://doi.org/10.1175/JAS-D-14-0354.1>.
- Rasmussen, R., and Coauthors, 1992: Winter Icing and Storms Project (WISP). *Bull. Amer. Meteor. Soc.*, **73**, 951–976, [https://doi.org/10.1175/1520-0477\(1992\)073<0951:WIASP>2.0.CO;2](https://doi.org/10.1175/1520-0477(1992)073<0951:WIASP>2.0.CO;2).
- Rauber, R. M., M. K. Macomber, D. M. Plummer, A. A. Rosenow, G. M. McFarquhar, B. F. Jewett, D. Leon, and J. M. Keeler, 2014: Finescale radar and airmass structure of the comma head of a continental winter cyclone: The role of three airstreams. *Mon. Wea. Rev.*, **142**, 4207–4229, <https://doi.org/10.1175/MWR-D-14-00057.1>.
- , S. M. Ellis, J. Vivekanandan, J. Stith, W.-C. Lee, G. M. McFarquhar, B. F. Jewett, and A. Janiszkeski, 2017: Finescale structures of a snowstorm over the northeastern United States: A first look at high-resolution HIAPER cloud radar observations. *Bull. Amer. Meteor. Soc.*, **98**, 253–269, <https://doi.org/10.1175/BAMS-D-15-00180.1>.
- Rosenow, A. A., D. M. Plummer, R. M. Rauber, G. M. McFarquhar, B. F. Jewett, and D. Leon, 2014: Vertical velocity and physical structure of generating cells and convection in the comma head region of continental winter cyclones. *J. Atmos. Sci.*, **71**, 1538–1558, <https://doi.org/10.1175/JAS-D-13-0249.1>.

- Ryzhkov, A., P. Zhang, H. Reeves, M. Kumjian, T. Tschallener, S. Trömel, and C. Simmer, 2016: Quasi-vertical profiles—a new way to look at polarimetric radar data. *J. Atmos. Oceanic Technol.*, **33**, 551–562, <https://doi.org/10.1175/JTECH-D-15-0020.1>.
- Schnaiter, M., E. Järvinen, A. Abdelmonem, and T. Leisner, 2018: PHIPS-HALO: The airborne Particle Habit Imaging and Polar Scattering probe—Part 2: Characterization and first results. *Atmos. Meas. Tech.*, **11**, 341–357, <https://doi.org/10.5194/amt-11-341-2018>.
- Smith, T. M., and Coauthors, 2016: Multi-Radar Multi-Sensor (MRMS) severe weather and aviation products: Initial operating capabilities. *Bull. Amer. Meteor. Soc.*, **97**, 1617–1630, <https://doi.org/10.1175/BAMS-D-14-00173.1>.
- Stark, D., B. A. Colle, and S. E. Yuter, 2013: Observed microphysical evolution for two East Coast winter storms and the associated snowbands. *Mon. Wea. Rev.*, **141**, 2037–2057, <https://doi.org/10.1175/MWR-D-12-00276.1>.
- Stechman, D. M., G. M. McFarquhar, R. M. Rauber, B. F. Jewett, and R. A. Black, 2020: Composite in situ microphysical analysis of all spiral vertical profiles executed within BAMEX and PECAN mesoscale convective systems. *J. Atmos. Sci.*, **77**, 2541–2565, <https://doi.org/10.1175/JAS-D-19-0317.1>.
- Szeto, K. K., and R. E. Stewart, 1997: Effects of melting on frontogenesis. *J. Atmos. Sci.*, **54**, 689–702, [https://doi.org/10.1175/1520-0469\(1997\)054<0689:EOMOF>2.0.CO;2](https://doi.org/10.1175/1520-0469(1997)054<0689:EOMOF>2.0.CO;2).
- Um, J., and Coauthors, 2018: Microphysical characteristics of frozen droplet aggregates from deep convective clouds. *Atmos. Chem. Phys.*, **18**, 16 915–16 930, <https://doi.org/10.5194/acp-18-16915-2018>.
- Vaillancourt, P. A., A. Tremblay, S. G. Cober, and G. A. Isaac, 2003: Comparison of aircraft observations with mixed-phase clouds simulations. *Mon. Wea. Rev.*, **131**, 656–671, [https://doi.org/10.1175/1520-0493\(2003\)131<0656:COAOWM>2.0.CO;2](https://doi.org/10.1175/1520-0493(2003)131<0656:COAOWM>2.0.CO;2).
- Waitz, F., M. Schnaiter, T. Leisner, and E. Järvinen, 2022: In-situ observation of riming in mixed-phase clouds using the PHIPS probe. *Atmos. Chem. Phys.*, **22**, 7087–7103, <https://doi.org/10.5194/acp-22-7087-2022>.
- Walker McLinden, M. L., A. M. Loftus, L. Li, and G. M. Heymsfield, 2021a: Application of nonuniform beam filling (NUBF) Doppler velocity error correction on airborne radar measurements. *IEEE Geosci. Remote Sens. Lett.*, **19**, 3509905, <https://doi.org/10.1109/LGRS.2021.3120647>.
- , L. Li, G. M. Heymsfield, M. Coon, and A. Emory, 2021b: The NASA GSFC 94-GHz airborne solid-state Cloud Radar System (CRS). *J. Atmos. Oceanic Technol.*, **38**, 1001–1017, <https://doi.org/10.1175/JTECH-D-20-0127.1>.
- Wang, Y., and Coauthors, 2020: Microphysical properties of generating cells over the Southern Ocean: Results from SOCRATES. *J. Geophys. Res. Atmos.*, **125**, e2019JD032237, <https://doi.org/10.1029/2019JD032237>.
- Wiesmueller, J. L., and S. M. Zubrick, 1998: Evaluation and application of conditional symmetric instability, equivalent potential vorticity, and frontogenetic forcing in an operational forecast environment. *Wea. Forecasting*, **13**, 84–101, [https://doi.org/10.1175/1520-0434\(1998\)013<0084:EAAOCS>2.0.CO;2](https://doi.org/10.1175/1520-0434(1998)013<0084:EAAOCS>2.0.CO;2).
- Wexler, R., and D. Atlas, 1959: Precipitation generating cells. *J. Atmos. Sci.*, **16**, 327–332, [https://doi.org/10.1175/1520-0469\(1959\)016<0327:PGC>2.0.CO;2](https://doi.org/10.1175/1520-0469(1959)016<0327:PGC>2.0.CO;2).